M2PDE: Compositional Generative Multiphysics and Multi-component PDE Simulation

Tao Zhang [1] **Zhenhai Liu** [1] **Feipeng Qi** [1] **Yongjun Jiao** [1] **Tailin Wu** [2]

Abstract

Multiphysics simulation, which models the interactions between multiple physical processes, and multi-component simulation of complex structures are critical in fields like nuclear and aerospace engineering. Previous studies use numerical solvers or ML-based surrogate models for these simulations. However, multiphysics simulations typically require integrating multiple specialized solvers—each for a specific physical process—into a coupled program, which introduces significant development challenges. Furthermore, existing numerical algorithms struggle with highly complex large-scale structures in multi-component simulations. Here we propose compositional <u>M</u>ultiphysics and <u>M</u>ulti-component <u>PDE</u> Simulation with Diffusion models (M2PDE) to overcome these challenges. During diffusion-based training, M2PDE learns energy functions modeling the conditional probability of one physical process/component conditioned on other processes/components. In inference, M2PDE generates coupled multiphysics and multi-component solutions by sampling from the joint probability distribution. We evaluate M2PDE on two multiphysics tasks—reaction-diffusion and nuclear thermal coupling—where it achieves more accurate predictions than surrogate models in challenging scenarios. We then apply it to a multi-component prismatic fuel element problem, demonstrating that M2PDE scales from single-component training to a 64-component structure and outperforms existing domain-decomposition and graph-based approaches. The code is at github.com/AI4Science-WestlakeU/M2PDE.

1. Introduction

Multiphysics simulation involves the concurrent modeling of multiple physical processes—such as heat conduction, fluid flow, and structural mechanics—within a single simulation framework to accurately capture the coupling effects between different physical processes. Similarly, multi-component simulation focuses on simulating complex structures composed of multiple similar components. Component is defined as: a repeatable basic unit that makes up a complete structure. For example, the reactor core typically consists of hundreds or thousands of fuel elements arranged in a square or hexagonal pattern. These simulations are essential across various scientific and engineering disciplines, including nuclear engineering (Ma et al., 2022; Chen et al., 2021), aerospace engineering (Candeo et al., 2011; Wang et al., 2023a), civil engineering (Sun et al., 2017; Meyer et al., 2022), and automotive industry (Ragone et al., 2021). Despite their significance, both multiphysics and multi-component partial differential equation (PDE) simulations share a common challenge: while simulating individual components or physical processes is relatively straightforward, modeling the entire system with all its interactions is vastly more complex.

Numerous numerical algorithms have been developed for multiphysics simulation, which are broadly categorized into loose coupling and tight coupling (Hales et al., 2015). Loose coupling solves each physical process independently, iteratively transferring solutions until convergence, using methods like operator splitting (MacNamara & Strang, 2016) and Picard iteration (Terlizzi & Kotlyar, 2022). Tight coupling solves all processes simultaneously in a large system (Knoll & Keyes, 2004), which can be more accurate but faces challenges such as high computational costs, varying spatial and temporal resolutions, and differing numerical methods across physical processes. Thus, loose coupling is more commonly used in engineering applications. In multi-component simulation, directly simulating the overall structure requires high computational cost and may encounter difficulties in convergence due to the increase in degrees of freedom. Substructure methods have been used in fields like nuclear engineering (Chen et al., 2021) and civil engineering (Sun et al., 2017) to reduce modeling and computational

costs for repetitive components.

Despite advances in numerical algorithms, several significant challenges remain in engineering applications. In multiphysics simulations, considerable time and effort are required to develop programs that couple different specialized solvers. Furthermore, the complexity of the system increases due to coupling, requiring more computing resources. While some studies employ machine learning-based surrogate models to accelerate simulations (Sobes et al., 2021; Park et al., 2021), these models still depend on coupled data for training, which necessitates the prior development of coupled numerical solution programs. In the case of multi-component simulations, the substructure method has primarily been applied to mechanical problems, with no widely applicable general method for multi-component systems. Consequently, current methods often rely on selecting representative units for detailed analysis or introducing simplifications to the overall structure, which may compromise the accuracy and scope of the simulations.

To address these challenges in engineering applications, we propose compositional <u>Multi</u>physics and <u>Multi</u>-component <u>PDE</u> Simulation with Diffusion models (M2PDE). The core innovation of M2PDE is its treatment of multiphysics and multi-component PDE simulations as generative probabilistic modeling, where interactions between multiple physical processes or components are captured through composing learned energy functions conditioned on others in a structured way. In multiphysics simulation, M2PDE generates coupled solutions (accounting for interactions between different physical processes) from decoupled data (assuming other fields are known and focused on solving a single field) by modeling the solutions of physical processes as a joint probability distribution. The solution for each individual process is treated as a conditional probability distribution, based on Bayes' theorem. By training diffusion models (Ho et al., 2020) on decoupled data, we capture these conditional distributions. During inference, the model combines these distributions and performs reverse diffusion to produce the coupled solution. For multi-component simulations, M2PDE models each component's solution as a conditional probability distribution using the local Markov property, conditioned on neighboring components. By training diffusion models on small structures, we create conditional models for individual components. During inference, reverse diffusion is applied iteratively across all components, yielding the solution for the entire structure. We have mathematically derived the principles why M2PDE can obtain coupled solutions and large structure solutions in Sections 3.1 and 3.2. A schematic of M2PDE is provided in Fig. 1.

We illustrate the promise of this approach through simplified problems in practical engineering, both of which are important in nuclear engineering and has widespread implications across engineering. First, we demonstrate its capability for multiphysics simulation by applying it to coupled reaction-diffusion equations and nuclear thermal coupling combined with conjugate heat transfer. Second, we verify its capability in multi-component simulation through thermal and mechanical analysis of prismatic fuel elements.

Concretely, our contributions are threefold: (1) We introduce a novel approach, M2PDE, for multiphysics and multi-component PDE simulations, framing the problem in terms of joint probabilistic modeling. By training on decoupled (small structure) training data, it can generate coupled (large structure) solutions. (2) We create and open-source benchmark datasets for both multiphysics and multi-component PDE simulations, providing a valuable resource for future research. (3) Our method demonstrates success in both domains. For multiphysics simulation, M2PDE accurately predicts coupled solutions in complex problems where surrogate models fail. In multi-component simulations, M2PDE, trained on single components, accurately predicts larger structures with up to 64 components.

2. Related Work

Multiphysics simulation. Most existing studies develop unified surrogate models for all physical processes by coupling solutions (Tang et al., 2024; Ren et al., 2020; Park et al., 2021; Wang et al., 2023b). For complex problems, programs for each physical process are typically independent. It is often feasible to establish a surrogate model for one specific physical process and then integrate it with other numerical programs (El Haber et al., 2022; Han et al., 2019). Alternatively, surrogate models can be constructed separately for each physical processes and iteratively converged through an iterative process (Sobes et al., 2021). Because the purpose of our algorithm is to infer coupled solutions through models trained with decoupled data, and establishing the surrogate model for all physical processes requires coupling solution training models, we adopt the method of establishing surrogate models for each physical process separately as the baseline to validate the proposed algorithm.

Multi-component simulation. To our knowledge, there do not exist utilized machine learning methods specifically designed for multi-component simulation. A relevant study is the CoAE-MLSim algorithm (Ranade et al., 2021). This algorithm combines neural networks with numerical iteration. It first partitions the computational domain into multiple subdomains, and then trains a neural network to learn the flux conversation between subdomains, similar to the domain decomposition algorithm (Chan & Mathew, 1994). During inference, the neural network with flux conservation is applied sequentially in each subdomain, looping until convergence. We further extend this algorithm to multi-component simulation and use it as a baseline. Besides, graph neural
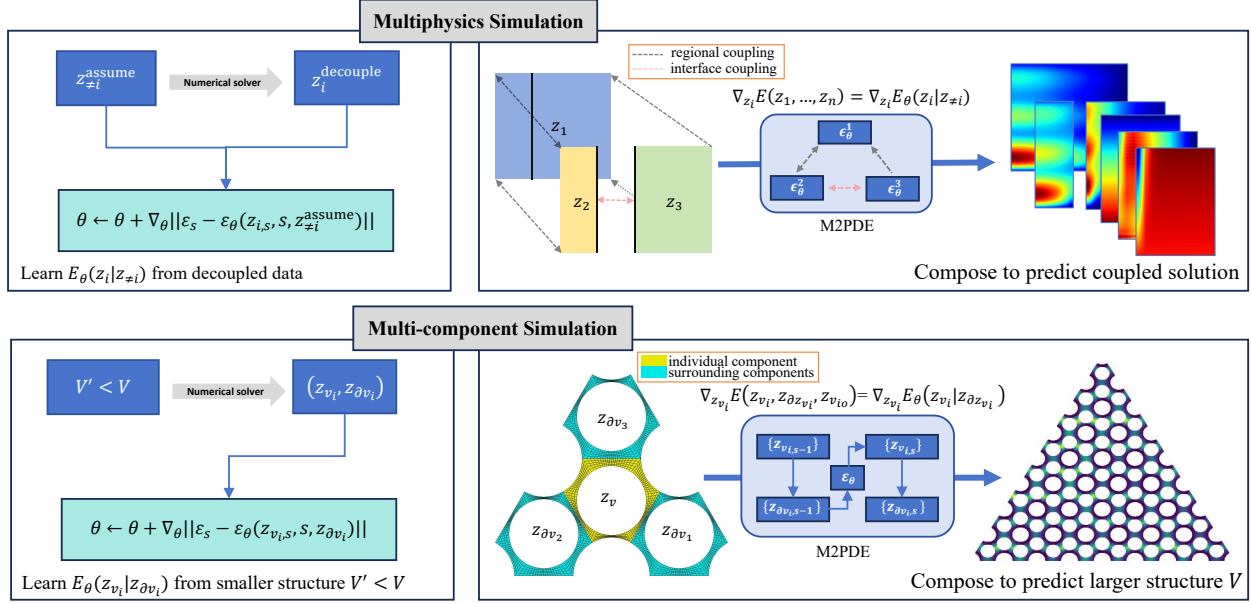
Figure 1. M2PDE schematic. Our proposed algorithm can use models trained with decoupled data to predict coupled solutions (top) and use models trained with small structure to predict large structures (here 64 components)(bottom).

network (GNN) (Wu et al., 2020; Fan et al., 2024) can learn on small graphs and inference on larger graphs (Xu et al., 2019); Graph Transformer (Kreuzer et al., 2021) employs the Laplacian matrix of a graph to characterize its structure, and by leveraging the Transformer architecture, it achieves learning on graphs. We also compare M2PDE with GNN and Graph Transformer.

Compositional models. Recent research has extensively explored the compositional combination of generative models for various applications, including image or video synthesis (Du et al., 2020; 2023; Po & Wetzstein, 2024; Yang et al., 2023), multimodal perception (Li et al., 2022), trajectory planning (Du et al., 2019; Urain et al., 2023), inverse design (Wu et al., 2024b), and data assimilation (Rozet & Louppe, 2023). A particularly effective approach for combining predictive distributions from local experts is the product of experts framework (Hinton, 2002; Cohen et al., 2020). Their focus is on how a single object is influenced by multiple factors, such as generating images that meet various requirements in image generation (Du et al., 2023) or enhancing the lift-to-drag ratio under the influence of two wings in inverse design (Wu et al., 2024b). However, our problem involves multiple objects, such as multiple physical processes and components, requiring the capture of interactions between these fields or components. Existing research is not applicable to multiphysics and multi-component PDE simulation. To the best of our knowledge, we are the first to introduce a compositional generative approach to multiphysics and multi-component PDE simulations, demonstrating how this framework enables generalization to far more

complex simulation tasks than those encountered during training.

3. Method

In this section, we introduce the principle of M2PDE solving multiphysics and multi-component PDE simulation in section 3.1 and section 3.2, respectively.

3.1. Multiphysics simulation

Consider a complex multiphysics simulation that consists of multiple physical processes : $z = (z_1, z_2, \ldots, z_N)$, each z_i represents the *trajectory* of one or more physical fields that belong to that specific i-th physical process. For example, the mechanics might contain both the stress and strain fields in three directions over a given time interval $[0, T]$. Each process z_i has its own governing equation which depends on other processes , and solving equations for other processes also requires that process. Therefore, all equations must be solved *simultaneously* to achieve the most accurate representation of the physical system.

Simulating all the processes z together can be challenging, while it will be simple if we simulate a single process z_i. By specifying the other processes $z_{\neq i} = (z_1, ..., z_{i-1}, z_{i+1}, ..., z_N)$ and the given outer inputs[1]

$$z_i = f(z_{\neq i}, C) \tag{1}$$

---

[1] In this paper, "outer inputs" refers to the inputs of the physical system.

where f is a numerical solver. Omitting the given condition C, then: $z_i = f(z_{\neq i})$. Now we consider the results of multiple physical processes as a joint probability distribution:

$$(z_1, z_2, ..., z_N) \sim p(z_1, z_2, ..., z_N) \tag{2}$$

For each process, we consider it as a conditional distribution: $z_i \sim p(z_i|z_{\neq i})$, which relates to the joint distribution via:

$$p(z_1, z_2, ..., z_N) = p(z_i|z_{\neq i})p(z_{\neq i}) \tag{3}$$

Writing the probability distribution in the form of (learnable) energy functions $E(z)$ (Du et al., 2023; LeCun et al., 2006), the energy functions relates to the joint probability of z, the conditional probability of z_i, and the marginal distribution of $z_{\neq i}$ respectively by:

$$\begin{cases} p(z) = \dfrac{1}{Z}e^{-E(z)} \\ p(z_i \mid z_{\neq i}) = \dfrac{1}{Z(z_{\neq i})}e^{-E(z_i|z_{\neq i})} \\ p(z_{\neq i}) = \dfrac{1}{Z_{\neq i}}e^{-E(z_{\neq i})} \end{cases} \tag{4}$$

where $Z, Z_{\neq i}$ are normalization coefficients (constants). Note that for $p(z_i|z_{\neq i})$, since $z_{\neq i}$ is the condition, the normalization $Z(z_{\neq i})$ depends on $z_{\neq i}$. Substituting Eq. 4 into Eq. 3, then taking logarithms of both sides, we have:

$$\begin{aligned} E(z) + \log Z &= [E(z_i \mid z_{\neq i}) + \log Z(z_{\neq i})] \\ &+ [E(z_{\neq i}) + \log Z_{\neq i}] \end{aligned} \tag{5}$$

Taking the derivative w.r.t. z_i on both sides, we have:

$$\nabla_{z_i} E(z_1, z_2, ..., z_N) = \nabla_{z_i} E(z_i|z_{\neq i}) \tag{6}$$

which uses the fact that $\log Z$, $\log Z_{\neq i}$, $\log Z(z_{\neq i})$, and $E(z_{\neq i})$ are all independent of z_i.

Eq. 6 is the foundation of our compositional multiphysics simulation method. We see that when sampling the joint distribution $p(z_1, z_2, ..., z_N)$, we can simply use the learned conditional diffusion model to sample each z_i, while using the estimated $z_{\neq i}^e$ of other physical processes as conditions. This means that to learn the multiphysics simulation of multiple physical processes $z_1, z_2, ..., z_N$, we no longer need to develop a coupled algorithm that simultaneously solves all physical processes. Instead, we can simply use decoupled solvers (each physical process is solved independently while treating the other physical processes as known) to generate data, learn the conditional distributions $p(z_i|z_{\neq i}) \propto e^{-E(z_i|z_{\neq i})}$, and in the inference time, sample from the joint distribution via Eq. 6, achieving multiphysics simulation. During training, the energy $E(z_i|z_{\neq i})$ is implicitly learned via the diffusion objective below, which learns the gradient of the energy:

$$L_{\text{MSE}} = ||\epsilon - \epsilon_\theta(\sqrt{1-\beta_s}z_i + \sqrt{\beta_s}\epsilon; z_{\neq i}, s)||_2^2 \tag{7}$$

where the denoising network $\epsilon_\theta(\cdot)$ corresponds to the gradient of the energy function $\nabla_z E_\theta(\cdot)$ (Du et al., 2023), $\epsilon \sim \mathcal{N}(0, I)$. During inference, we sample from the joint distribution $p(z_1, z_2, ...z_N)$ via (Ho et al., 2020):

$$\begin{aligned} z_{i,s-1} &= \frac{1}{\sqrt{\alpha_s}}\left(z_{i,s} - \frac{1-\alpha_s}{\sqrt{1-\overline{\alpha}_s}}\epsilon_\theta^i(z_{i,s} \mid z_{\neq i}^e, s)\right) \\ &+ \sigma_s w, \ \ w \sim \mathcal{N}(0, I) \end{aligned} \tag{8}$$

$$z_i^e = \frac{1}{\sqrt{\overline{\alpha}_s}}\left(z_{i,s} - \sqrt{1-\overline{\alpha}_s}\epsilon_\theta^i(z_{i,s} \mid z_{\neq i}^e, s)\right) \tag{9}$$

for $s = S, S-1, ...1$ and $i = 1, 2, ...n$. Here, z_i^e represents the estimated value for the ith field z_i, $z_{\neq i}^e = (z_1^e, ...z_{i-1}^e, z_{i-1}^e, ...z_n^e)$, and σ_s is the noise level, the superscript e represents estimation.

This iterative method is similar to the Expectation-Maximization (EM) algorithm (Moon, 1996), refining each variable's estimation based on current estimates of others. An external loop can be added to repeat the diffusion model's inference, using the previous step's physical fields to improve the initial estimate. The ablation study about hyperparameters K, λ and the estimation method are discussed in Appendix F. The algorithm is shown in Algorithm 1. Line 2 is the external loop, while lines 6 to 11 represent the denoising cycle of the diffusion model. In each diffusion step, the physical physical processes are updated sequentially, with $z_{\neq i}$ using the estimated physical processes that have already been updated at this diffusion step.

3.2. Multi-component simulation

Consider a complex structure that is composed of many components: $V = v_1 \cup v_2 \cup \ldots \cup v_N$, and the solution in each component v_i is z_{v_i}. It should be noted that v_i represents an entity here, and if there are multiple physical processes on this entity, it is also a multiphysics problem. Each component shares similarities and is arranged in a specific pattern, like an array, to compose this complex structure. Simulating the entire structure V can be challenging while simulating an individual component v_i is easier. By specifying the boundary condition $z_{\partial v_i}$, the given outer inputs C, and the geometry v_i of component v_i, we can compute z_{v_i}:

$$z_{v_i} = f(z_{\partial v_i}, C, v_i) \tag{10}$$

where f is a numerical solver. The outer inputs C and geometry v_i are given conditions, $z_{\partial v_i}$ is boundary conditions. Omitting the given condition, then: $z_{v_i} = f(z_{\partial v_i})$. Then we divide the whole geometry V to three parts: $V = v_i \cup \partial v_i \cup v_{io}$, where v_{io} represents other parts of V except $v_i \cup \partial v_i$. The solution of the whole geometry V can be written as the following probability distribution:

$$(z_{v_i}, z_{\partial v_i}, z_{v_{io}}) \sim p(z_{v_i}, z_{\partial v_i}, z_{v_{io}}) \tag{11}$$

Algorithm 1 Algorithm for multiphysics simulation by M2PDE.

---

input Compositional set of diffusion model $\epsilon_\theta^i(z_{i,s}, C, s), i = 1, 2, ..., N$, outer inputs C, diffusion step S, number of external loops K, number of physical processes N.

1: $z_i^e \sim \mathcal{N}(0, I)$ // initialize estimated fields z_i^e
   // An external loop to improve the estimated fields z_i^e:
2: **for** $k = 1, ..., K$ **do**
3:     // initialize each physical fields z_i, for i in $1, ..., N$
4:     $\hat{z}_i^e \leftarrow z_i^e$ // previous estimated fields $\hat{z}_i^e$
5:     $z_i^e \sim \mathcal{N}(0, \mathbf{I})$ // current estimated fields z_i^e
6:     $z_{i,S} \sim \mathcal{N}(0, \mathbf{I})$ // intial physical fields z_i
       // denoising cycle of diffusion model:
7:     **for** $s = S, ..., 1$ **do**
8:         $\lambda = 1 - \frac{s}{S}$ if $k > 1$ else 1 // define the weights of $\hat{z}_i^e$ and z_i^e
           // loops for each physical process:
9:         **for** $i = 1, ..., N$ **do**
10:             $w \sim \mathcal{N}(0, \mathbf{I})$
               // use weighted estimated fields as conditions for single step denoising:
11:             $z_{i,s-1} = \frac{1}{\sqrt{\alpha_s}}(z_{i,s} - \frac{1-\alpha_s}{\sqrt{1-\bar{\alpha}_s}}\epsilon_\theta^i(z_{i,s} \mid \lambda z_{\neq i}^e + (1-\lambda)\hat{z}_{\neq i}^e, C, s)) + \sigma_s w$
               // update the estimation of current field:
12:             $z_i^e = \frac{1}{\sqrt{\bar{\alpha}_s}}(z_{i,s} - \sqrt{1 - \bar{\alpha}_s}\epsilon_\theta^i(z_{i,s} \mid \lambda z_{\neq i}^e + (1-\lambda)\hat{z}_{\neq i}^e, C, s))$
13:         **end for**
14:     **end for**
15: **end for**
output $z_{1,0}, z_{2,0}, ..., z_{N,0}$

Consider the complex structure as an undirected graph $G = (V, E)$, and the random variable z_{v_i} is the property of component v_i. The graph G satisfies the local Markov property: A variable is conditionally independent of all other variables given its neighbors. Thus, z_{v_i} satisfies

$$(z_{v_i} \perp z_{V \setminus N[v_i]})|z_{\partial v_i} \qquad (12)$$

Here ∂v_i is the set of neighbors of v_i, $N[v_i] = v_i \cup \partial v_i$, and $V \setminus N[v_i] = v_{io}$. By using this property of Markov random field, $p(z_{v_i}, z_{\partial v_i}, z_{v_{io}})$ can be written as:

$$p(z_{v_i}, z_{\partial v_i}, z_{v_{io}}) = p(z_{v_i}|z_{\partial v_i})p(z_{v_{io}}|z_{\partial v_i})p(z_{\partial v_i}) \quad (13)$$

Writing the probability distribution in the form of energy, and through the same derivation as in Section 3.1, we obtain:

$$\nabla_{z_{v_i}} E(z_{v_i}, z_{\partial v_i}, z_{v_{io}}) = \nabla_{z_{v_i}} E(z_{v_i}|z_{\partial v_i}) \qquad (14)$$

Therefore, when sampling the joint distribution $p(z_{v_1}, z_{v_2}, ..., z_{v_N})$, we can simply use the learned conditional diffusion model to sample each z_{v_i}, while using

the estimated $z_{\partial v_i}^e$ as conditions. The multi-component simulation can be achieved using an algorithm similar to multiphysics simulation. Since each z_{v_i} is inferred with the same model, it can be processed together, improving inference efficiency by eliminating the need for additional loops for each physical process. We provide Alg. 2 in Appendix A for multi-component simulation. Additionally, we use the assumption of Markov random fields in the derivation. The rationality of this assumption and the application scenarios of the algorithm are discussed in Appendix J.

Our proposed framework of multiphysics simulation in Section 3.1 and multi-component simulation in Section 3.2, constitute our full method of compositional Multiphysics and Multi-component PDE Simulation with Diffusion models (M2PDE). It circumvents the development of coupled programs that requires huge development efforts, and achieves multiphysics and multi-component PDE simulation by composing the learned conditional energy functions according to the variable dependencies. Below, we test our method's capability in challenging engineering problems.

4. Experiments

In the experiments, we aim to answer the following questions: (1) Can M2PDE predict coupled solutions (accounting for interactions between different physical processes) from models trained in decoupled data (assuming other processes are known and focus on solving a single process)? (2) Can M2PDE predict large structure solutions from a model trained in small structure data? (3) Can M2PDE outperform surrogate model[2] in both tasks? To answer these questions, we conduct experiments to assess our algorithm's performance on two problems across three scenarios. In Section 4.1, we solve the reaction-diffusion equation. While it's not a classic multiphysics coupling issue since both quantities are part of concentration fields, we consider them as separate physical processes to validate the capability of M2PDE for multiphysics simulation. Section 4.2 explores a complex nuclear engineering scenario, involving various types of coupling: region, interface, strong, weak, unidirectional, and bidirectional to further test the algorithm's capacity to handle multiphysics simulation. Section 4.3 simplifies actual nuclear engineering problems to evaluate the algorithm's effectiveness with multi-component simulation. Each ex-

---

[2]The surrogate model in this article refers to a neural network that directly maps system inputs to outputs in one step, unlike diffusion models that generate outputs step-by-step through denoising. For multiphysics problems, surrogate models are trained separately for each physical field using decoupled data, and obtain coupled solutions through iteration.. For multi-component problems, surrogate models use domain decomposition concepts, predicting each component iteratively based on surrounding components to achieve convergence.

Table 1. Relative L2 norm of error on reaction-diffusion equation for multiphysics simulation.

method	u decoupled	coupled	v decoupled	coupled
surrogate + FNO	0.0669	0.0600	0.0080	0.0320
M2PDE (ours) + FNO	0.0270	**0.0290**	0.0102	**0.0264**
surrogate + U-Net	0.0152	0.0184	0.0039	**0.0174**
M2PDE (ours) + U-Net	0.0119	**0.0141**	0.0046	**0.0174**

periment uses two network architectures, training both with their respective diffusion and surrogate models for comparison, employing consistent hyperparameters and settings to ensure fairness. The computational domains of experiment 1 and experiment 2 are on regular meshes, using Fourier neural operator (FNO) (Li et al., 2021; Lim et al., 2023) and U-Net (Ronneberger et al., 2015) as network architectures. The computational domain of experiment 3 is on a finite element mesh, using Geo-FNO (Li et al., 2023) and Transolver (Wu et al., 2024a) as the network architecture. Additionally, in experiment 3, we also compare M2PDE with graph neural networks GIN (Xu et al., 2019) Graph transformer SAN (Kreuzer et al., 2021) and MeshGraphNet (Pfaff et al., 2020).

To highlight the difference between training and testing data, Appendix G calculates the Wasserstein distances between decoupled and coupled data in multiphysics problems, as well as between small and large structural data in multi-component problem, and visualizes them. In Appendix K, we conduct a comparison of our dataset with existing scientific datasets (Takamoto et al., 2022). As another contribution to the community, we also open-source the data at here to facilitate future method development of multiphysics and multi-component PDE simulations.

4.1. Reaction-diffusion

Reaction-diffusion (RD) equations have found wide applications in the analysis of pattern formation, including chemical reactions. This experiment uses the 1D FitzHugh-Nagumo reaction-diffusion equation (Rao et al., 2023), it has two concentration fields: u, v, the governing equations are presented in Eq. 15. The objective is to predict the system's evolution under different initial conditions. The training data consists of decoupled data, where other physical processes are assumed and treated as inputs to solve the equations governing the current physical process . Gaussian random field (Bardeen et al., 1986) is employed to generate the other physical processes and initial conditions, and numerical algorithms are used to compute the solution of the current physical process. The validation data similarly consists of decoupled data not used during training. The test data consists of coupled solutions obtained using fully coupled algorithms. Further details on the datasets, equation,

network architecture, and training process are provided in Appendix B.

$$
\begin{cases}
\dfrac{\partial u}{\partial t} = \mu_u \Delta u + u - u^3 - v + \alpha, x \in [0,1], t \in [0,5] \\
\dfrac{\partial v}{\partial t} = \mu_v \Delta v + (u-v)\beta, x \in [0,1], t \in [0,5] \\
[u,v] = [u_0, v_0], x \in [0,1], t = 0
\end{cases}
$$
(15)

Table 1 presents the relative L2 norm (L2 norm of prediction error divided by L2 norm of the ground-truth) in predictions made by surrogate model and M2PDE on a validation set of decoupled data and a test set of coupled data. For FNO, the prediction error for u is comparable between M2PDE and surrogate models on decoupled data; however, M2PDE shows a significantly larger error in predicting v, which is four times that of the surrogate model. As a result, the error in predicting the coupled solution for v is greater than that of the surrogate model, while the error for u is lower. For U-Net, the prediction errors for u and v are similar between M2PDE and surrogate models on decoupled data, but M2PDE achieves a lower error for the coupled solution.

This straightforward experiment tests the correctness of M2PDE but shows no significant advantages over the surrogate model. However, the surrogate model fails in solving more complex problems, which will be discussed in the next section.

4.2. Nuclear thermal coupling

This experiment evaluates M2PDE's performance in handling various physical processes and coupling modes, including regional and interface coupling, strong and weak coupling, and unidirectional and bidirectional coupling. The focus is on nuclear-thermal coupling in transient conditions for plate fuel elements, using a simplified pin cell analysis with a transient disturbance modeled as a change in neutron flux density at the boundary. This physical system requires solving neutron physics, heat conduction, and flow heat transfer equations, taking into account negative feedback between neutron physics and temperature, unidirectional coupling from fluid to neutron field, and strong interface coupling between solid and fluid. The goal is to predict the system's evolution under different neutron boundary

$$\begin{cases} \frac{1}{v}\frac{\partial \phi(x,y,t)}{\partial t} = D\Delta\phi + (v\Sigma_f - \Sigma_a(T))\phi, x \in [0, L_s + L_f], y \in [0, L_y], t \in [0,5] \\ \phi(0,y,t) = f(y,t) \\ \phi(L_s + L_f, y, t) = \phi(x,0,t) = \phi(x,L_y,t) = 0 \end{cases} \quad (16)$$

$$\begin{cases} \frac{\rho c_p T_s(x,y,t)}{\partial t} = \nabla k_s \nabla T_s + A\phi_s, x \in [0, L_s], y \in [0, L_y], t \in [0,5] \\ \frac{\partial T_s(x,0,t)}{\partial y} = \frac{\partial T_s(x,L_y,t)}{\partial y} = 0 \\ T_s(L_s,y,t) = T_f(L_s,y,t) \end{cases} \quad (17)$$

$$\begin{cases} \nabla \cdot \vec{u} = 0, x \in [L_s, L_s + L_f], y \in [0, L_y], t \in [0,5] \\ \rho\left(\frac{\partial \vec{u}}{\partial t} + \vec{u} \cdot \nabla \vec{u}\right) = -\nabla p + \mu\nabla^2 \vec{u} + \vec{f}, x \in [L_s, L_s + L_f], y \in [0, L_y], t \in [0,5] \\ \rho c_p\left(\frac{\partial T_f}{\partial t} + \vec{u} \cdot \nabla T_f\right) = k_f\nabla^2 T, x \in [L_s, L_s + L_f], y \in [0, L_y], t \in [0,5] \\ k_f\frac{\partial T_f(L_s,y,t)}{\partial x} = k_s\frac{\partial T_s(L_s,y,t)}{\partial x} \end{cases} \quad (18)$$

conditions. The geometric and coupling relationships are illustrated in Fig. 2. The governing equations for the coupled evolution of neutron flux (ϕ), solid temperature (T_s), and fluid temperature, pressure, and velocity ($T_f, p, \vec{u}$) are presented in Eq. 16, Eq. 17, and Eq. 18, respectively.

(a) Solid temperature. (b) Fluid temperature.

Figure 3. Comparison of prediction results between M2PDE and surrogate model. The surrogate model fails on the test set of the coupled scenario.
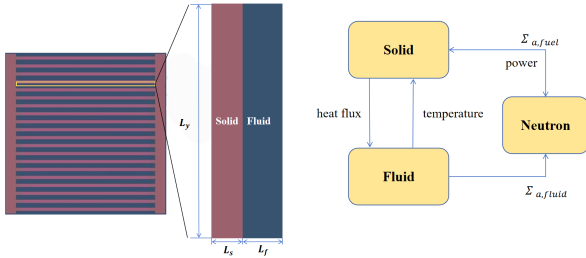

Figure 2. Geometric structure (left); Coupling relationship between different physical processes (right).

Generating estimated physical fields in this two-dimensional time series problem with three physical processes is challenging using Gaussian random fields. To address this, we employ a pre-iteration method for data generation. The validation dataset consists of decoupled data not used during training, while the test dataset comprises coupled data. Coupled data is computed using the operator splitting iterative algorithm (MacNamara & Strang, 2016), which exchanges information between physical processes at each time step. Additional details on the datasets, network architecture, and training process can be found in Appendix C.

Table 2 displays the relative prediction errors of surrogate models and M2PDE on a validation set of decoupled data
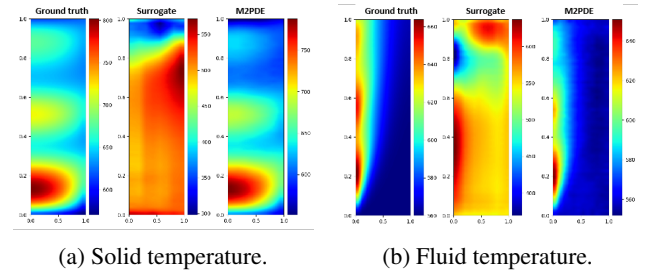
and a test set of coupled data. In single physical process prediction (decoupled data), surrogate models outperform M2PDE. However, in predicting the coupled solution, all surrogate models fail except for the neutron physics field, with the predicted solid and fluid temperature fields shown in Fig. 3 (for more visualizations, see Fig. 6). The neutron physics field remains relatively accurate because the feedback from solid and fluid temperatures is weak and primarily driven by external input boundary conditions. In contrast, solid temperature and fluid fields are significantly influenced by other physical processes, leading to non-physical predictions due to the lack of iterative process data during training. In comparison, M2PDE more accurately captures the morphology of coupled solutions and demonstrates higher accuracy. In addition, we further use DDIM (Song et al., 2021) to accelerate sampling and compare the operational efficiency of different methods. M2PDE achieves an acceleration of up to **29-fold speedup**, with detailed information in Appendices H and I.
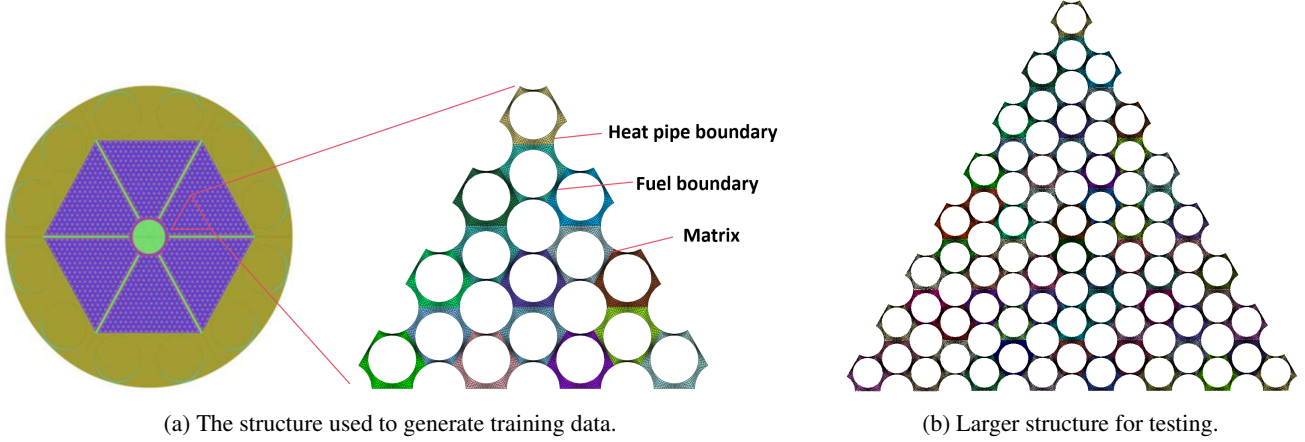
7

(a) The structure used to generate training data.

(b) Larger structure for testing.

Figure 4. In (a), the left figure shows the entire reactor. The right figure illustrates a portion of the reactor core. This structure composed of 16 fuel elements is used to generate training data. (b) is a large structure composed of 64 elements used for testing.

Table 2. Relative L2 norm of prediction error on nuclear thermal coupling for multiphysics simulation. The unit is 1×10^{-2}.

	neutron		solid		fluid	
method	decoupled	coupled	decoupled	coupled	decoupled	coupled
surrogate + FNO	0.251	22.1	0.0445	31.8	0.106	10.2
M2PDE (ours) + FNO	0.738	**8.42**	0.175	**9.72**	0.615	**7.31**
surrogate + U-Net	0.181	4.45	0.0800	18.2	0.0927	8.03
M2PDE (ours) + U-Net	0.741	**1.38**	0.140	**2.75**	0.228	**3.86**

4.3. Prismatic fuel element

This experiment tests the ability of M2PDE to solve multi-component simulation problems, focusing on the thermal and mechanical analysis of prismatic fuel elements for a new type of reactor (Ma et al., 2022). The reactor core consists of three components: fuel, matrix, and heat pipe. Since engineering focuses mainly on the matrix, we consider the fuel and fluid as boundary conditions for analysis. Different heat fluxes will be assigned to the fuel boundary to simulate various heat release behaviors of the fuel rods. The aim is to train a model that predicts its temperature T and strain $\varepsilon_x, \varepsilon_y$ based on the solutions of its three neighbors and its heat flux.

The training data originate from a medium structure simulation that includes 16 fuel elements; hence, a single simulation data point can generate 16 training data. The well-trained model will be tested on two structures: one is the medium structure used for data generation, and the other is a large structure containing 64 fuel elements, as shown in Fig. 4. Further details on the datasets, network architecture, and training process are provided in Appendix D.

Table 3 presents the prediction relative errors of surrogate model and M2PDE across three tasks: a single fuel element, a medium structure of 16 fuel elements, and a large struc-

ture of 64 fuel elements. The average relative error of strain $\varepsilon_x, \varepsilon_y$ is denoted as ε. GIN, SAN, and MeshGraphNet learn on small graphs with 16 components and test on large graphs with 64 components. Due to the uniformity of graph structures in all training data and the fact that SAN learns a global relationship, SAN fails to predict larger structures. GIN and MeshGraphNet are capable of learning local relationships, thereby successfully handling larger-scale structures. Specifically, MeshGraphNet achieves the lowest error when learning structures with 16 components. However, when extrapolating to even larger structures, M2PDE exhibits lower error than MeshGraphNet.

Subsequently, a comparative analysis between the surrogate model and M2PDE has been conducted. The surrogate model performs better in predicting a single component, but for medium structure, M2PDE outperforms it. It's important to note that the surrogate model's predictions occasionally diverge, necessitating adjustments to the relaxation factor to maintain stability. For the large structure, U-Net in the surrogate model demonstrates better stability, while the FNO model continues to diverge even after relaxation factor adjustments. M2PDE is very stable and accurate, and no divergence phenomenon has been observed. In term of strain, the relative error of M2PDE has been reduced by 41% Compared with the surrogate model. In addition,

Table 3. Relative L2 norm of prediction error on prismatic fuel element experiment, for single-component and 16-component (medium) and 64-component (large) simulations. The unit is 1×10^{-2}.

method	single		16-component		64-component	
	T	ε	T	ε	T	ε
GIN	-	-	1.96	3.18	4.63	7.02
SAN	-	-	0.114	16.5	1.00×10^2	1.18×10^4
MeshGraphNet	-	-	0.0583	0.427	1.28	2.40
surrogate + Geo-FNO	0.0883	0.195	**0.337**	2.59	divergent	divergent
M2PDE (ours) + Geo-FNO	0.139	0.459	0.338	**2.42**	**0.950**	**3.52**
surrogate + Transolver	0.0764	0.251	0.314	1.13	1.25	3.31
M2PDE (ours) + Transolver	0.144	0.339	**0.288**	**1.01**	**0.793**	**2.07**

we further use DDIM to accelerate sampling and compare the operational efficiency of different methods. M2PDE achieves an acceleration of up to **41-fold speedup**, with detailed information in Appendices H and I.

5. Limitation and future work

There are also several limitations of our proposed M2PDE that provide exciting opportunities for future work. Firstly, in multiphysics simulation, although the M2PDE trained on decoupled data can predict coupled solutions more accurately than baseline surrogate models, the prediction errors are still higher compared to single physical processes predictions. In addition, there is a certain gap in accuracy compared to models trained through coupled data, as shown in Appendix E. Future efforts can focus on improving dataset generation, training methods, and incorporating physical information to boost accuracy. Secondly, we plan to explore additional accelerated sampling algorithms, aiming to significantly improve efficiency while maintaining prediction accuracy. Lastly, while the experiments in this paper have simplified certain aspects of real-world engineering problems to focus on key issues and improve research efficiency, future work will aim to apply this method to more complex practical engineering problems to further validate its effectiveness and practicality.

6. Conclusion

This work presents M2PDE as a novel method for multiphysics and multi-component PDE simulations, driven by the needs of real-world engineering applications. In multiphysics scenarios, models trained on decoupled data can predict coupled solutions, while in multi-component simulations, models trained on small structures can extrapolate to larger ones. We develop three datasets to validate M2PDE and compare it to the surrogate model method. Results show that M2PDE effectively predicts coupled solutions in multiphysics simulations where surrogate models fail, and exhibits greater accuracy in predicting larger structures in multi-component simulations. We believe this approach provides a new approach to address multiphysics and multi-component PDE simulations, important across science and engineering.

Impact Statement

This paper presents work whose goal is to advance the field of Machine Learning. There are many potential societal consequences of our work, none which we feel must be specifically highlighted here.

References

Bardeen, J. M., Bond, J., Kaiser, N., and Szalay, A. The statistics of peaks of gaussian random fields. *Astrophysical Journal, Part 1 (ISSN 0004-637X), vol. 304, May 1, 1986, p. 15-61. SERC-supported research.*, 304:15–61, 1986.

Candeo, A., Ducassy, C., Bocher, P., and Dughiero, F. Multiphysics modeling of induction hardening of ring gears for the aerospace industry. *IEEE Transactions on Magnetics*, 47(5):918–921, 2011.

Chan, T. F. and Mathew, T. P. Domain decomposition algorithms. *Acta numerica*, 3:61–143, 1994.

Chen, W., Wang, D., and Zhang, Y. Seismic fragility analysis of nuclear power plants based on the substructure method. *Nuclear Engineering and Design*, 382:111389, 2021. ISSN 0029-5493. doi: https://doi.org/10.1016/j.nucengdes.2021.111389. URL https://www.sciencedirect.com/science/article/pii/S0029549321003411.

Cohen, S., Mbuvha, R., Marwala, T., and Deisenroth, M. Healing products of gaussian process experts. In *Interna-*

tional Conference on Machine Learning, pp. 2068–2077. PMLR, 2020.

Du, Y., Lin, T., and Mordatch, I. Model based planning with energy based models. *CORL*, 2019.

Du, Y., Li, S., and Mordatch, I. Compositional visual generation with energy based models. In *Advances in Neural Information Processing Systems*, 2020.

Du, Y., Durkan, C., Strudel, R., Tenenbaum, J. B., Dieleman, S., Fergus, R., Sohl-Dickstein, J., Doucet, A., and Grathwohl, W. S. Reduce, reuse, recycle: Compositional generation with energy-based diffusion models and mcmc. In *International conference on machine learning*, pp. 8489–8510. PMLR, 2023.

El Haber, G., Viquerat, J., Larcher, A., Ryckelynck, D., Alves, J., Patil, A., and Hachem, E. Deep learning model to assist multiphysics conjugate problems. *Physics of Fluids*, 34(1), 2022.

Fan, S., Hitt, A. L., Tang, M., Sadigh, B., and Zhou, F. Accelerate microstructure evolution simulation using graph neural networks with adaptive spatiotemporal resolution. *Machine Learning: Science and Technology*, 5(2):025027, 2024.

Feydy, J., Séjourné, T., Vialard, F.-X., Amari, S.-i., Trouve, A., and Peyré, G. Interpolating between optimal transport and mmd using sinkhorn divergences. In *The 22nd International Conference on Artificial Intelligence and Statistics*, pp. 2681–2690, 2019.

Gong, D., Huang, S., Wang, G., and Wang, K. Heat transfer calculation on plate-type fuel assembly of high flux research reactor. *Science and Technology of Nuclear Installations*, 2015(1):198654, 2015.

Gupta, J. K. and Brandstetter, J. Towards multi-spatiotemporal-scale generalized PDE modeling. *Transactions on Machine Learning Research*, 2023. ISSN 2835-8856. URL https://openreview.net/forum?id=dPSTDbGtBY.

Hales, J., Tonks, M., Gleicher, F., Spencer, B., Novascone, S., Williamson, R., Pastore, G., and Perez, D. Advanced multiphysics coupling for lwr fuel performance analysis. *Annals of Nuclear Energy*, 84:98–110, 2015.

Han, Z., Rahul, and De, S. A deep learning-based hybrid approach for the solution of multiphysics problems in electrosurgery. *Computer Methods in Applied Mechanics and Engineering*, 357:112603, 2019. ISSN 0045-7825. doi: https://doi.org/10.1016/j.cma.2019.112603. URL https://www.sciencedirect.com/science/article/pii/S0045782519304797.

Hinton, G. E. Training products of experts by minimizing contrastive divergence. *Neural computation*, 14(8):1771–1800, 2002.

Ho, J., Jain, A., and Abbeel, P. Denoising diffusion probabilistic models. In Larochelle, H., Ranzato, M., Hadsell, R., Balcan, M., and Lin, H. (eds.), *Advances in Neural Information Processing Systems*, volume 33, pp. 6840–6851. Curran Associates, Inc., 2020. URL https://proceedings.neurips.cc/paper_files/paper/2020/file/4c5bcfec8584af0d967f1ab10179ca4b-Paper.pdf.

Icenhour, C., Keniley, S., DeChant, C., Permann, C., Lindsay, A., Martineau, R., Curreli, D., and Shannon, S. Multiphysics object oriented simulation environment (moose). Technical report, Idaho National Lab.(INL), Idaho Falls, ID (United States), 2018.

Knoll, D. and Keyes, D. Jacobian-free newton–krylov methods: a survey of approaches and applications. *Journal of Computational Physics*, 193(2):357–397, 2004. ISSN 0021-9991. doi: https://doi.org/10.1016/j.jcp.2003.08.010. URL https://www.sciencedirect.com/science/article/pii/S0021999103004340.

Kreuzer, D., Beaini, D., Hamilton, W., Létourneau, V., and Tossou, P. Rethinking graph transformers with spectral attention. *Advances in Neural Information Processing Systems*, 34:21618–21629, 2021.

LeCun, Y., Chopra, S., Hadsell, R., Ranzato, M., Huang, F., et al. A tutorial on energy-based learning. *Predicting structured data*, 1(0), 2006.

Li, S., Puig, X., Paxton, C., Du, Y., Wang, C., Fan, L., Chen, T., Huang, D.-A., Akyürek, E., Anandkumar, A., et al. Pre-trained language models for interactive decision-making. *Advances in Neural Information Processing Systems*, 35:31199–31212, 2022.

Li, Z., Kovachki, N. B., Azizzadenesheli, K., liu, B., Bhattacharya, K., Stuart, A., and Anandkumar, A. Fourier neural operator for parametric partial differential equations. In *International Conference on Learning Representations*, 2021. URL https://openreview.net/forum?id=c8P9NQVtmnO.

Li, Z., Huang, D. Z., Liu, B., and Anandkumar, A. Fourier neural operator with learned deformations for pdes on general geometries. *Journal of Machine Learning Research*, 24(388):1–26, 2023.

Lim, J. H., Kovachki, N. B., Baptista, R., Beckham, C., Azizzadenesheli, K., Kossaifi, J., Voleti, V., Song, J., Kreis, K., Kautz, J., et al. Score-based diffusion models in function space. *arXiv preprint arXiv:2302.07400*, 2023.

Ma, Y., Liu, J., Yu, H., Tian, C., Huang, S., Deng, J., Chai, X., Liu, Y., and He, X. Coupled irradiation-thermal-mechanical analysis of the solid-state core in a heat pipe cooled reactor. *Nuclear Engineering and Technology*, 54 (6):2094–2106, 2022.

MacNamara, S. and Strang, G. *Operator Splitting*, pp. 95–114. Springer International Publishing, Cham, 2016. ISBN 978-3-319-41589-5. doi: 10.1007/978-3-319-41589-5_3. URL https://doi.org/10.1007/978-3-319-41589-5_3.

Meyer, P. P., Bonatti, C., Tancogne-Dejean, T., and Mohr, D. Graph-based metamaterials: Deep learning of structure-property relations. *Materials & Design*, 223:111175, 2022. ISSN 0264-1275. doi: https://doi.org/10.1016/j.matdes.2022.111175. URL https://www.sciencedirect.com/science/article/pii/S0264127522007973.

Moon, T. K. The expectation-maximization algorithm. *IEEE Signal processing magazine*, 13(6):47–60, 1996.

Park, T.-R., Park, H., Kim, K., Im, C.-N., and Cho, J.-H. Heat and weight optimization methodology of thermal batteries by using deep learning method with multiphysics simulation. *Energy Conversion and Management*, 236:114033, 2021.

Pfaff, T., Fortunato, M., Sanchez-Gonzalez, A., and Battaglia, P. Learning mesh-based simulation with graph networks. In *International conference on learning representations*, 2020.

Po, R. and Wetzstein, G. Compositional 3d scene generation using locally conditioned diffusion. In *2024 International Conference on 3D Vision (3DV)*, pp. 651–663. IEEE, 2024.

Ragone, M., Yurkiv, V., Ramasubramanian, A., Kashir, B., and Mashayek, F. Data driven estimation of electric vehicle battery state-of-charge informed by automotive simulations and multi-physics modeling. *Journal of Power Sources*, 483:229108, 2021.

Ranade, R., Hill, C., He, H., Maleki, A., Chang, N., and Pathak, J. A composable autoencoder-based iterative algorithm for accelerating numerical simulations. *CoRR*, abs/2110.03780, 2021. URL https://arxiv.org/abs/2110.03780.

Rao, C., Ren, P., Wang, Q., Buyukozturk, O., Sun, H., and Liu, Y. Encoding physics to learn reaction–diffusion processes. *Nature Machine Intelligence*, 5(7):765–779, 2023.

Ren, T., Wang, L., Chang, C., and Li, X. Machine learning-assisted multiphysics coupling performance optimization in a photocatalytic hydrogen production system. *Energy Conversion and Management*, 216:112935, 2020.

Ronneberger, O., Fischer, P., and Brox, T. U-net: Convolutional networks for biomedical image segmentation. In *Medical image computing and computer-assisted intervention–MICCAI 2015: 18th international conference, Munich, Germany, October 5-9, 2015, proceedings, part III 18*, pp. 234–241. Springer, 2015.

Rozet, F. and Louppe, G. Score-based data assimilation. *Advances in Neural Information Processing Systems*, 36: 40521–40541, 2023.

Sobes, V., Hiscox, B., Popov, E., Archibald, R., Hauck, C., Betzler, B., and Terrani, K. Ai-based design of a nuclear reactor core. *Scientific reports*, 11(1):19646, 2021.

Song, J., Meng, C., and Ermon, S. Denoising diffusion implicit models. In *International Conference on Learning Representations*, 2021. URL https://openreview.net/forum?id=St1giarCHLP.

Sun, B., Gu, Q., Zhang, P., and Ou, J. A practical numerical substructure method for seismic nonlinear analysis of tall building structures. *The Structural Design of Tall and Special Buildings*, 26(16):e1377, 2017.

Takamoto, M., Praditia, T., Leiteritz, R., MacKinlay, D., Alesiani, F., Pflüger, D., and Niepert, M. Pdebench: An extensive benchmark for scientific machine learning. In *Advances in Neural Information Processing Systems*, volume 35, pp. 1596–1611, 2022.

Tang, Z., Zhao, S., Li, J., Zuo, Y., Tian, J., Tang, H., Fan, J., and Zhang, G. Optimizing the chemical vapor deposition process of 4h–sic epitaxial layer growth with machine-learning-assisted multiphysics simulations. *Case Studies in Thermal Engineering*, 59:104507, 2024.

Terlizzi, S. and Kotlyar, D. A perturbation-based acceleration for monte carlo–thermal hydraulics picard iterations. part ii: Application to 3d pwr-based problems. *Annals of Nuclear Energy*, 166:108713, 2022.

Urain, J., Li, A., Liu, P., D'Eramo, C., and Peters, J. Composable energy policies for reactive motion generation and reinforcement learning. *The International Journal of Robotics Research*, 42(10):827–858, 2023.

Van der Maaten, L. and Hinton, G. Visualizing data using t-sne. *Journal of machine learning research*, 9(11), 2008.

Wang, C., han Song, L., Yuan, Z., and sheng Fan, J. State-of-the-art ai-based computational analysis in civil engineering. *Journal of Industrial*

Information Integration, 33:100470, 2023a. ISSN 2452-414X. doi: https://doi.org/10.1016/j.jii.2023.100470. URL https://www.sciencedirect.com/science/article/pii/S2452414X23000432.

Wang, J., Jiang, H., Chen, G., Wang, H., Lu, L., Liu, J., and Xing, L. Integration of multi-physics and machine learning-based surrogate modelling approaches for multi-objective optimization of deformed gdl of pem fuel cells. *Energy and AI*, 14:100261, 2023b.

Wu, H., Luo, H., Wang, H., Wang, J., and Long, M. Transolver: A fast transformer solver for pdes on general geometries. In *International Conference on Machine Learning*, 2024a.

Wu, T., Maruyama, T., Wei, L., Zhang, T., Du, Y., Iaccarino, G., and Leskovec, J. Compositional generative inverse design. In *The Twelfth International Conference on Learning Representations*, 2024b. URL https://openreview.net/forum?id=wmX0CqFSd7.

Wu, Z., Pan, S., Chen, F., Long, G., Zhang, C., and Philip, S. Y. A comprehensive survey on graph neural networks. *IEEE transactions on neural networks and learning systems*, 32(1):4–24, 2020.

Xu, K., Hu, W., Leskovec, J., and Jegelka, S. How powerful are graph neural networks? In *International Conference on Learning Representations*, 2019. URL https://openreview.net/forum?id=ryGs6iA5Km.

Yang, M., Du, Y., Dai, B., Schuurmans, D., Tenenbaum, J. B., and Abbeel, P. Probabilistic adaptation of text-to-video models. *arXiv preprint arXiv:2306.01872*, 2023.

A. Algorithm for multi-component simulation.

Multi-component simulation first requires training a diffusion model to predict the solution of the current component based on the solutions of its neighboring components. Additionally, it is necessary to define the connectivity of all components and the function f to update the surrounding components' solutions for each component. The multi-component simulation algorithm is presented in Algorithm 2. Lines 6 to 11 are the denoising cycle of the diffusion model, in each diffusion step, the solutions of each component are updated together.

Algorithm 2 Algorithm for multi-component simulation by M2PDE

---

input A diffusion model $\epsilon_\theta(z_{\partial v_i}, C, s)$, outer inputs C, diffusion step S, number of external loops K, number of component
   N, connectivity of all components adj, update function $f(z_{v_1}, ..., z_{v_N}, \mathrm{adj})$ of $z_{\partial v}$.
1: $z_{v_i}^e \sim \mathcal{N}(0, I)$ // initialize estimated solution for each component v_i
   // Add an external loop to improve $z_{v_i}^e$:
2: **for** $k = 1, ..., K$ **do**
3:      // initialize each component z_{v_i}, for i in $1, ..., N$
4:      $\hat{z}_{v_i}^e \leftarrow z_{v_i}^e$ // update previous estimated solutions for each component $\hat{z}_{v_i}^e$
5:      $z_{v_i}^e \sim \mathcal{N}(0, \mathbf{I})$ // initialize current estimated solutions for each component z_i^e
6:      $z_{v_i, S} \sim \mathcal{N}(0, \mathbf{I})$ // initialize solutions for each component z_{v_i}
      // denoising cycle of diffusion model:
7:      **for** $s = S, ..., 1$ **do**
8:          $\lambda = 1 - \frac{s}{S}$ if $k > 1$ else 1 // define the weights of $\hat{z}_i^e$ and z_i^e
9:          $z_{\partial v} = f(z_{v_1}^e, ..., z_{v_N}^e, \mathrm{adj})$ // update the solutions of surrounding components for each z_{v_i}
10:         $w \sim \mathcal{N}(0, \mathbf{I})$
          // use weighted estimated solutions as conditions for single step denoising,
          // update all components together:
11:         $z_{v_i, s-1} = \frac{1}{\sqrt{\alpha_s}}(z_{v_i, s} - \frac{1 - \alpha_s}{\sqrt{1 - \overline{\alpha}_s}}\epsilon_\theta(z_{v_i, s} \mid \lambda z_{\partial v_i}^e + (1 - \lambda)\hat{z}_{\partial v_i}^e, C)) + \sigma_s w$
          // update the estimated solutions of all components together
12:         $z_{v_i}^e = \frac{1}{\sqrt{\overline{\alpha}_s}}(z_{v_i, s} - \sqrt{1 - \overline{\alpha}_s}\epsilon_\theta(z_{v_i, s} \mid \lambda z_{v_i}^e + (1 - \lambda)\hat{z}_{\partial v_i}^e, C))$
13:     **end for**
14: **end for**
output $z_{v_1, 0}, z_{v_2, 0}, ..., z_{v_N, 0}$

B. Additional details for reaction-diffusion

This section provides additional details for Section 4.1.

Dataset. We employed the solve_ivp function in Python to solve the reaction-diffusion equations. The coefficients μ_u, μ_v, α, and β of Eq. 18 are set to 0.01, 0.05, 0.1, and 0.25, respectively. The spatial mesh consisted of $n_x = 20$ points, the time step is adaptively controlled by the algorithm, but only outputs the results of 10 time steps. To train the data for a single physical process, it was necessary to assume the initial conditions of the other physical processes and the current field. For instance, training u required assumptions about u_0 and v. The dimension of u_0 is $[n_x]$, which was generated using a one-dimensional Gaussian random field, and v has dimensions $[n_t, n_x]$, and was generated by sampling a one-dimensional Gaussian random field n_t times. Similarly, training v also requires preparation of v_0 and u.

Model structure. The 2D U-Net and 2D FNO serve as both the surrogate and M2PDE. U-Net consists of modules: a downsampling encoder, a middle module, and an upsampling decoder. The encoder and decoder comprise four layers, each with three residual modules and downsampling/upsampling convolutions, with the third module incorporating attention mechanisms. The middle module also contains three residual modules, with attention mechanisms included in the second module. The input data is encoded into a hidden dimension before undergoing sequential downsampling and upsampling. FNO consists of three modules: a lift-up encoder, n FNO layers, and a projector decoder. Each FNO layer includes a spectral convolution, a spatial convolution, and a layer normalization. The surrogate model predicts the evolution of the current physical process using its initial conditions and those of other physical processes. Its input dimension is [b, 1, 10, 20] and output dimension is [b, 1, 10, 20]. The diffusion model has an input dimension of [b, 2, 10, 20] and an output dimension of [b, 1, 10, 20], with b representing the batch size. The shape of initial condition of [b, 1, 1, 20] and will repeat to align the

---

Algorithm 3 Surrogate model combination algorithm for multiphysics simulation.

---

input Compositional set of surrogate model $\epsilon_\theta^i(z_{\neq i}, C), i = 1, 2, ..., N$, outer inputs C, maximum number of iterations M, tolerance $\epsilon_{\max}$, relaxation factor α.
1: Initialize constant fields $z_i, i = 1, ..., N, m = 0$
2: **while** $m < M$ and $\epsilon > \epsilon_{max}$ **do**
3:    $m = m + 1$
4:    **for** $i = 1, ..., N$ **do**
5:       $\hat{z}_i = z_i$
6:       $z_i = \alpha\epsilon_\theta^i(z_{\neq i}, C) + (1 - \alpha)\hat{z}_i$
7:    **end for**
8:    $\epsilon = L_1(z_i - \hat{z}_i), i = 1, ..., N$
9: **end while**
output $z_1, z_2, ..., z_N$

---

required shape. The diffusion step of the diffusion model is set to 250. More details are shown in Table 4.

Training. The surrogate model and M2PDE are trained similarly, with further details in Table 5.

Inference. The hyperparameter K is set to 2. The surrogate models' combination algorithm in experiments 1 and 2 is identical, as demonstrated in Alg 3. The relaxation factor α is set to 0.5.

Table 4. Hyperparameters of model architecture for reaction-diffusion task.

Hyperparameter name	u	v
Hyperparameters for U-Net architecture:		
Channel expansion factor	(1,2)	(1,2)
Number of downsampling layers	2	2
Number of upsampling layers	2	2
Number of residual blocks for each layer	3	3
Hidden dimension	24	24
Hyperparameters for FNO architecture:		
FNO width	24	24
number of FNO layer	4	4
FNO mode	[6,12]	[6,12]
padding	[8,8]	[8,8]

Table 5. Hyperparameters of training for reaction-diffusion task.

Hyperparameters for U-Net and FNO training	u and v
Loss function	MSE
Number of examples for training dataset	10^4
Total number of training steps (surrogate; diffusion)	$10^5; 2 \times 10^5$
Gradient accumulate every per epoch	2
learning rate	10^{-4}
Batch size	256

C. Additional details for nuclear thermal coupling

This section provides additional details for Section 4.2.

Problem description. The goal of this problem is to predict the performance of plate-type fuel assembly under transient conditions. A typical pin cell in JRR-3M fuel assembly (Gong et al., 2015) is adopted as the computational domain, as shown in Fig. 2. For simplicity, the cladding in the fuel plate is omitted here without losing the representativeness of its

14

multiphysics coupling feature. U-Zr alloy and lead-bismuth fluid are adopted as fuel and coolant materials, respectively. Their physical property parameters can be found in the repository. We consider a single-group diffusion equation for the neutron physics process and employ an incompressible fluid model for coolant modeling. Temperature fields in solid and fluid can influence the macroscopic absorption cross-section in the neutron physics equation, while neutron flux affects the heat source in the fuel domain. Conjugate heat transfer occurs at the interface between the fluid and solid domains. While the feedback of temperature on neutrons is inherently complex, a linear negative feedback is assumed for simplicity. The governing equations are presented in Eq. 16, Eq. 17, and Eq. 18.

Here v is neutrons / per fission, D is the diffusion coefficient of the neutron, Σ_f, Σ_a are the fission and absorption cross-section, respectively, and we only consider the feedback of temperature on the absorption cross-section Σ_a here. k_s, k_f are the conductivity of solid and fluid, respectively, both being functions of T.

Dataset. We utilize the open-source finite element software MOOSE (Multiphysics Object-Oriented Simulation Environment) (Icenhour et al., 2018) to tackle the nuclear thermal coupling problem. The solid temperature field uses a mesh of [64, 8], the fluid fields have a mesh of [64, 12], and the neutron physics field employs a mesh of [64, 20]. The neutron physics and solid temperature fields are calculated using the finite element method at mesh points, while the fluid domain uses the finite volume method at mesh centers. Interpolation is applied to align the neutron physics and solid temperature values with the fluid fields. The time step is adaptively controlled by the algorithm, but only outputs the results of 16 time steps. So the input dimensions for the surrogate models of neutron physics field, solid temperature field, and fluid fields are [b, 2, 16, 64, 20], [b, 2, 16, 64, 8], and [b, 1, 16, 64, 12], respectively. The input dimensions for the diffusion model of the three fields are [b, 3, 16, 64, 20], [b, 3, 16, 64, 8], and [b, 5, 16, 64, 12], respectively. The output dimensions of the three fields are [b, 1, 16, 64, 20], [b, 1, 16, 64, 8], and [b, 4, 16, 64, 12], respectively.

As noted, assuming the distribution of physical field data in high-dimensional problems is challenging. We recommend a pre-iteration method for data generation. Initially, we assume constant values for all other physical fields and calculate the current field. This process repeats until all fields are computed. If there are n physical fields, pre-iteration requires n - 1 calculations plus one iteration for data generation, totaling $2n$ - 1 calculations. To accelerate data generation, the most time-consuming field can be excluded from pre-iteration. In this problem, the fluid fields' computation time is approximately three times that of the other fields, so it is excluded from pre-iteration. The process begins by assuming constant fluid fields and solid temperatures to calculate the neutron physics field, followed by using the resulting neutron physics field and assumed fluid fields' temperature to calculate the solid temperature. The data generation proceeds sequentially with calculations for the fluid fields, neutron physics field, and solid temperature field. Through this process, the input datasets for all physical fields are not constant fields, but rather fields with distribution information after one iteration.

Model structure. The 3D U-Net and 3D FNO serve as both the surrogate model and M2PDE, using a layer design identical to the 2D. For regional coupling, concatenation is directly applied to the channel dimension using the concat function. In contrast, for interface coupling, dimensions must be replicated to align spatially before concatenation. The conditioning of the diffusion step for FNO is operating in spectrum space (Gupta & Brandstetter, 2023), which is better than in the original space for this problem. The diffusion step of the diffusion model is set to 250. More details are shown in Table 6.

Training. The surrogate model and M2PDE are trained similarly, but training neutron physics fields using M2PDE requires more time to converge, with further details in Table 7.

Inference. The hyperparameter K is set to 2. The relaxation factor for surrogate model α is set to 0.5.

Detailed results. Fig. 5 llustrates how the relative errors are distributed along the x, y, t direction. Overall, the neutron field exhibits a relatively uniform distribution of errors along all three directions. In x direction, the error in both the solid and the fluid slightly increases near their interface, likely due to coupling effects in this region. Along the y direction, the solid temperature error gradually increases with distance, whereas the fluid error shows the opposite trend, which may be related to the distinct thermal and physical properties of the two media. Fig. 6 presents the results of predicting various physical fields using the last time step surrogate model and M2PDE + U-Net on the final test data. The neutron physics field and solid temperature field are represented by ϕ and T_s, respectively. The fluid fields include four physical quantities: T_f, P, u_x, u_y, totaling six quantities. Since the neutron physics field and the u_y component of the fluid fields are less influenced by other physical processes, the surrogate model can still make predictions, but the accuracy is lower than that of the M2PDE. Besides, the surrogate model has failed to predict the other physical processes. In contrast, M2PDE continues to provide relatively accurate predictions, although some distortions are observed in certain regions.

Table 6. Hyperparameters of model architecture for nuclear thermal coupling task.

Hyperparameter name	neutron	solid	fluid
Hyperparameters for U-Net architecture			
Channel Expansion Factor	(1,2,4)	(1,2,4)	(1,2,4)
Number of downsampling layers	3	3	3
Number of upsampling layers	3	3	3
Number of residual blocks for each layer	3	3	3
Hidden dimension	8	8	16
Hyperparameters for FNO architecture			
FNO width	8	8	16
number of FNO layer	3	3	3
FNO mode	[6,16,8]	[6,16,4]	[6,16,6]
padding	[8,8,8]	[8,8,8]	[8,8,8]

Table 7. Hyperparameters of training for nuclear thermal coupling task.

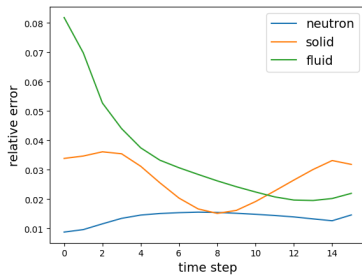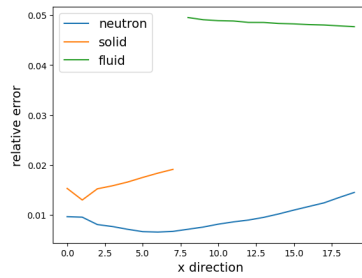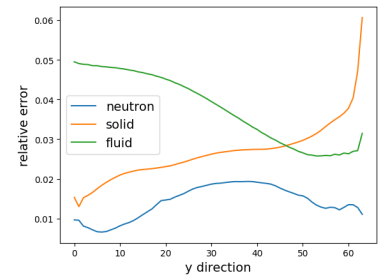| Hyperparameters for U-Net and FNO training	neutron&solid&fluid
Loss function	MSE
Number of examples for training dataset	5×10^3
Total number of training steps (surrogate; diffusion)	$10^5; 2 \times 10^5$
Gradient accumulate every per epoch	2
learning rate	10^{-4}
Batch size	32

(a) t direction.   (b) x direction.   (c) y direction.

Figure 5. The distribution of errors along the x, y, and t directions.

16

(a) ϕ.

(b) T_s.
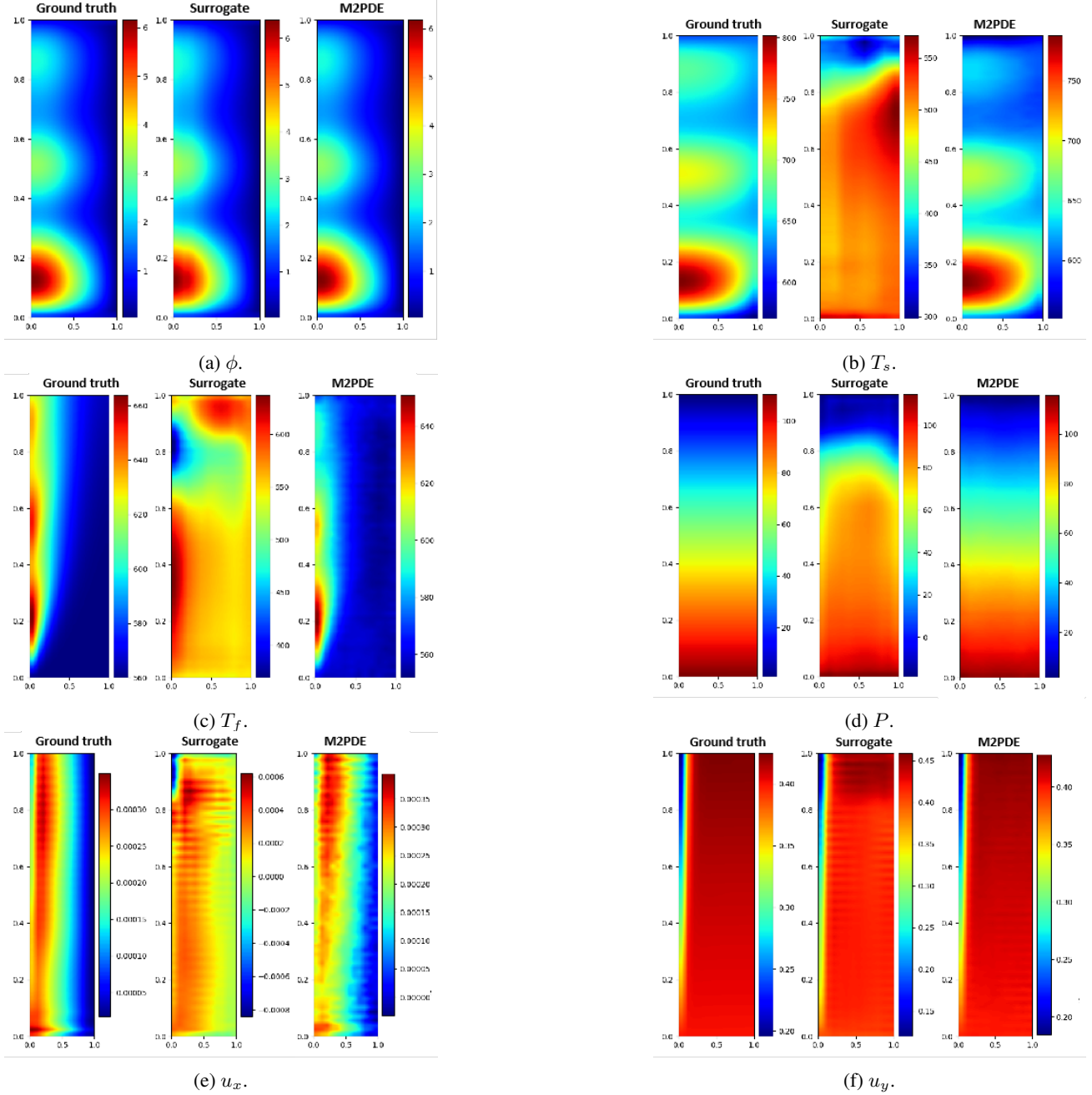
(c) T_f.

(d) P.

(e) u_x.

(f) u_y.

Figure 6. Comparison of surrogate model and M2PDE for predicting all physical fields.

D. Additional details for prismatic fuel element

This section provides additional details for Section 4.3.

Problem description. This problem aims to predict the thermal and mechanical performance of prismatic fuel elements in heat pipe reactor (Ma et al., 2022) at different source power. The reactor core is stacked up using a hexagonal prism SiC matrix, with multiple holes dispersed in the matrix for containing fuel elements and heat pipes as shown in Fig. 7. The SiC matrix plays a role in locating the fuel and heat pipes at expected positions in the core. The entire structure consists of two basic components, one oriented upwards and the other downwards, as illustrated in Fig. 8. Fission energy released in fuel elements is dissipated using heat pipes. Both the fuel elements and heat pipes are considered as boundaries here, and only the more concerned matrix behavior is analyzed in the demonstration. Only strain is predicted here since stress can be

derived from the mechanical constitutive equation, and displacement is obtained through strain integration. The analysis uses the plane strain assumption ($\varepsilon_z = 0$) and excludes irradiation effects, simplifying it to a steady-state problem.
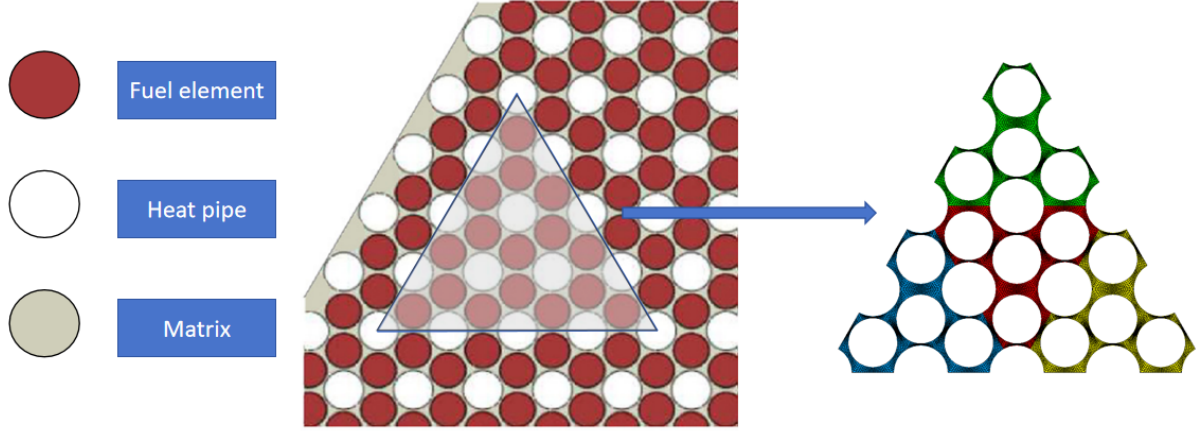

Figure 7. Schematic of heat pipe reactor core structure. The left figure shows a partial structure of the entire reactor, with multiple holes dispersed in the matrix for containing fuel elements and heat pipes. The right figure shows how to select a medium structure for analysis from the overall structure.
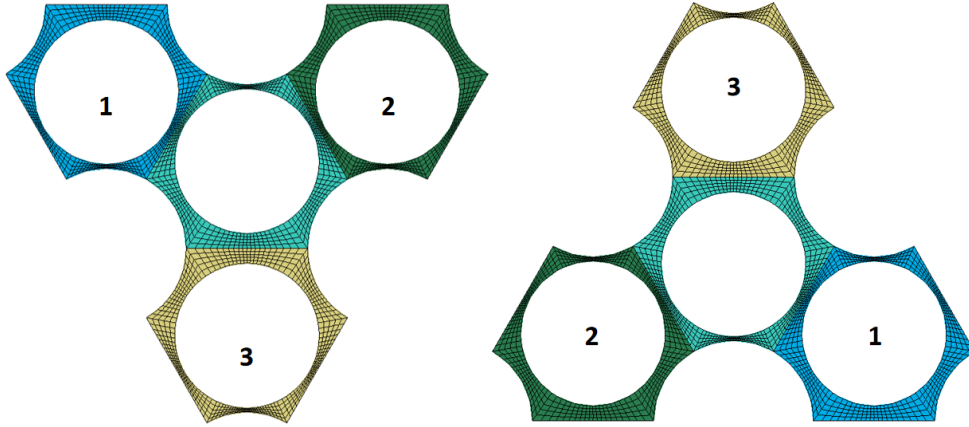

Figure 8. Two basic components: one facing upwards (left) and the other facing downwards (right).

Dataset. We use MOOSE to calculate the thermal and mechanical problems. The training data comes from a medium structure simulation with 16 fuel elements, allowing each simulation to generate 16 training data, as shown in Fig. 4. This structure is chosen because a fundamental component, along with its neighboring components, is entirely contained within the interior, which is where most components that need to be predicted in large structures are located. When generating data, the heat flux density is uniformly sampled from the range $[10^5, 10^6]$ W/m. A free boundary condition is randomly assigned to one edge, while symmetric boundary conditions are applied to the remaining two edges. Each fundamental component is uniformly meshed with 804 points, each requiring the prediction of three physical quantities. To predict the central component, the heat flux density of this component and the coordinates of each mesh point are concatenated with data from its three neighboring components, yielding an input dimension of [b, 804, 15] for the diffusion model and [b, 804, 12] for the surrogate model, where b is the batch size. The output dimension is [b, 804, 3]. The sequence of neighboring elements is consistent, with the downward-facing center element being the upward-facing center element rotated by 180 degrees. This arrangement is illustrated in Fig. 8. Boundary conditions are considered only for symmetric and free types, represented as [0, 1, 1] and [0, 0, 0], respectively, and are replicated to a dimension of [804, 3].

18

Algorithm 4 Surrogate model combination algorithm for multi-component simulation.

---

input A surrogate model $\epsilon_\theta(z_{\partial v}, C)$, outer inputs C, maximum number of iterations M, tolerance ϵ_{max}, relaxation factor α.

1: Initialize constant fields $z_{v_i}, i = 1, ..., N, m = 0$
2: **while** $m < M$ and $\epsilon > \epsilon_{max}$ **do**
3:     $m = m + 1$
4:     **for** $i = 1, ..., N$ **do**
5:         $\hat{z}_{v_i} = z_{v_i}$
6:         $z_{v_i} = \alpha \epsilon_\theta(z_{\partial v_i}, C) + (1 - \alpha)\hat{z}_{v_i}$
7:     **end for**
8:     $\epsilon = L_1(z_{\partial v_i} - \hat{z}_{\partial v_i}), i = 1, ..., N$
9: **end while**
output $z_{\partial v_1}, z_{\partial v_2}, ..., z_{\partial v_N}$

Model structure. The Geo-FNO and Transolver serve as both the surrogate model and M2PDE. Geo-FNO enhances FNO for irregular meshes using three modules: a geometry encoder that converts physical fields from irregular to latent uniform meshes, FNO functioning in latent space, and a geometry decoder that transforms physical fields from the uniform mesh back to the original irregular mesh. We utilize a 2D Geo-FNO that transforms into a 2D uniform mesh. Transolver is designed to tackle complex structural simulation problems involving numerous mesh points by learning the intrinsic physical states of the discretized domain. Given a mesh set with N points and C features per point, the network first assigns each mesh point to M potential slices, transforming the shape from $N \times C$ to $M \times N \times C$. It then applies spatially weighted aggregation, resulting in a shape of $M \times C$. Self-attention is used to capture intricate correlations among different slices, after which the data is transformed back to the mesh points. The conditioning of diffusion step for Geo-FNO is also operating in spectrum space (Gupta & Brandstetter, 2023). More details about the network can be found in (Wu et al., 2024a). The setting of hyperparameters is shown in Table 8. The diffusion step of the diffusion model is set to 250.

Training. The surrogate model and M2PDE are trained similarly, but training M2PDE requires more time to converge, with further details in Table 9.

Inference. This problem uses the same neural network to predict the performance of all elements, allowing for simultaneous updates of the physical fields and enhancing inference speed. This method applies to both diffusion and surrogate models. The surrogate models' combination algorithm for mult-component simulation is demonstrated in Alg 4, the relaxation factor α is set to 0.5. The hyperparameter K is set to 3.

Detailed results. Fig. 9 and Fig. 10 compares the results of predicting the large structure using the surrogate model and M2PDE + Transolver. Because the surrogate model of FNO fails in predicting large structures, only the results of M2PDE + FNO are provided in Fig. 11. The strain is only displayed in the x-direction due to its similarity in both x and y. The error graph indicates that M2PDE offers more accurate predictions.

Graph neural network and Graph Transformer configuration. For GIN, SAN and MeshGraphNet, each component is treated as a node in the graph, with training conducted on a small graph of 16-component, and ultimately tested on a larger graph of 64-component. Compared with the surrogate model and M2PDE, they use only the system's input as input features. In contrast, the surrogate model and M2PDE enrich its input by incorporating the solutions from the surrounding component, thereby improving accuracy, as demonstrated in Table 3. The input to the GIN, SAN and MeshGraphNet is the heat flux density and boundary conditions of each component, and the output is the physical quantities at all grid points on the component. GIN updates the nodes on the graph through the graph structure, whereas SAN captures graph structural information by inputting the eigenvalues and eigenvectors of the graph Laplacian matrix into a transformer. The training settings of GIN, SAN and MeshGraphNet are consistent with the M2PDE. We have adjusted the number of network layers and the size of hidden layers to obtain the model with optimal performance.

(a) Surrogate model when predicting T.

(b) M2PDE when predicting T.
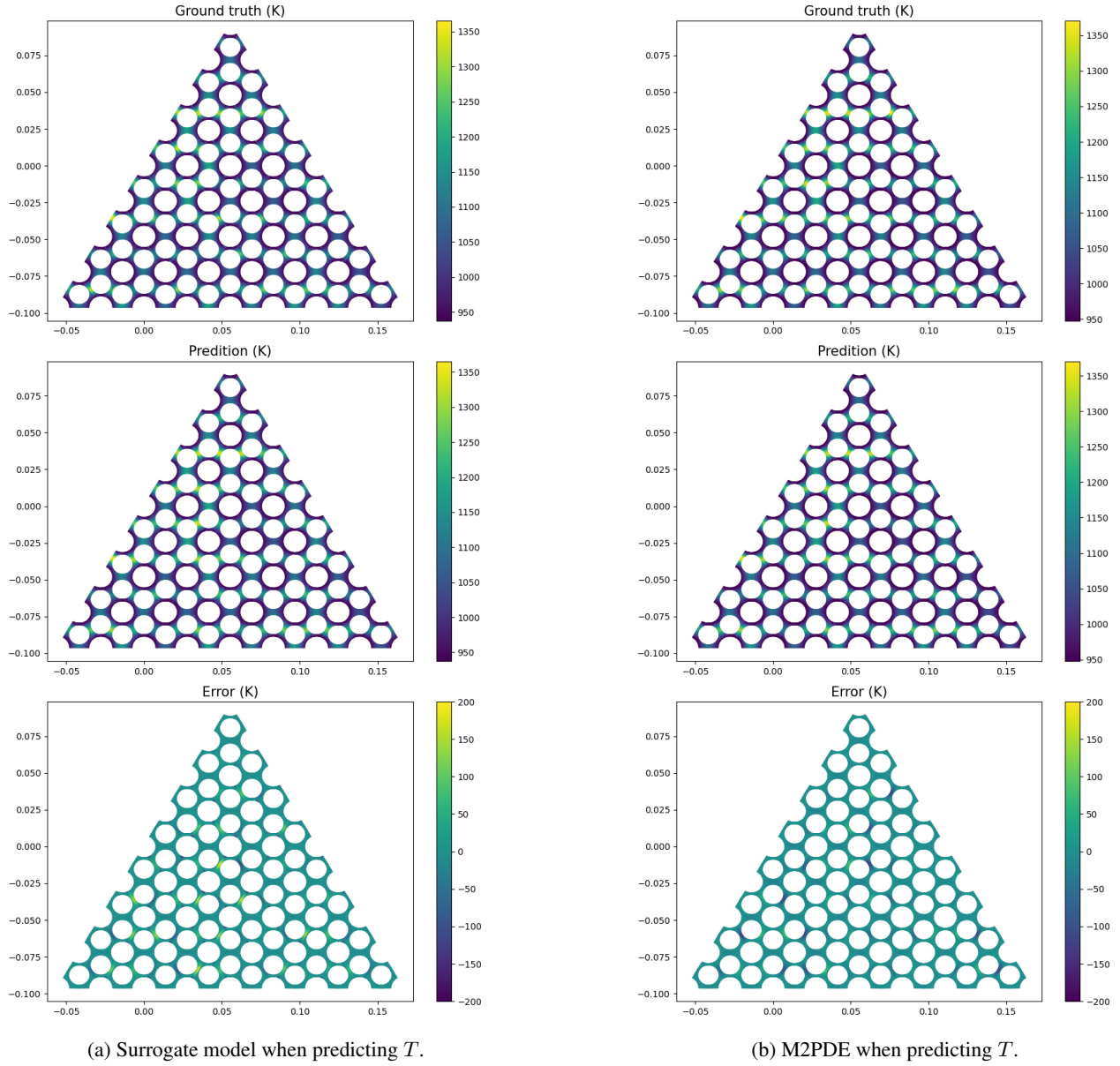
Figure 9. Comparison of surrogate models and M2PDE + Transolver for predicting the temperature of large structures.

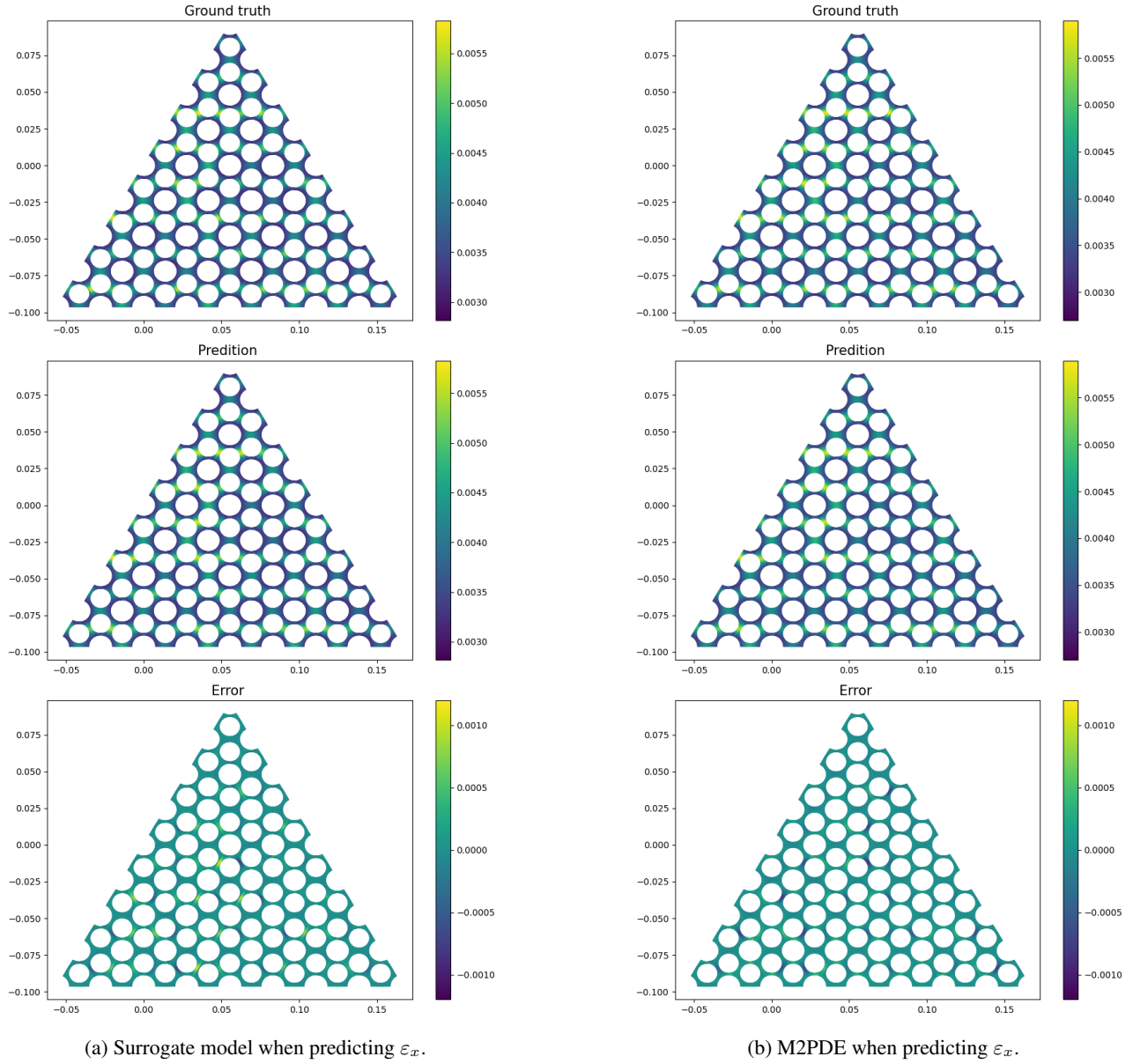(a) Surrogate model when predicting ε_x.

(b) M2PDE when predicting ε_x.

Figure 10. Comparison of surrogate models and M2PDE + Transolver for predicting the strain of large structures.

(a) M2PDE when predicting T.
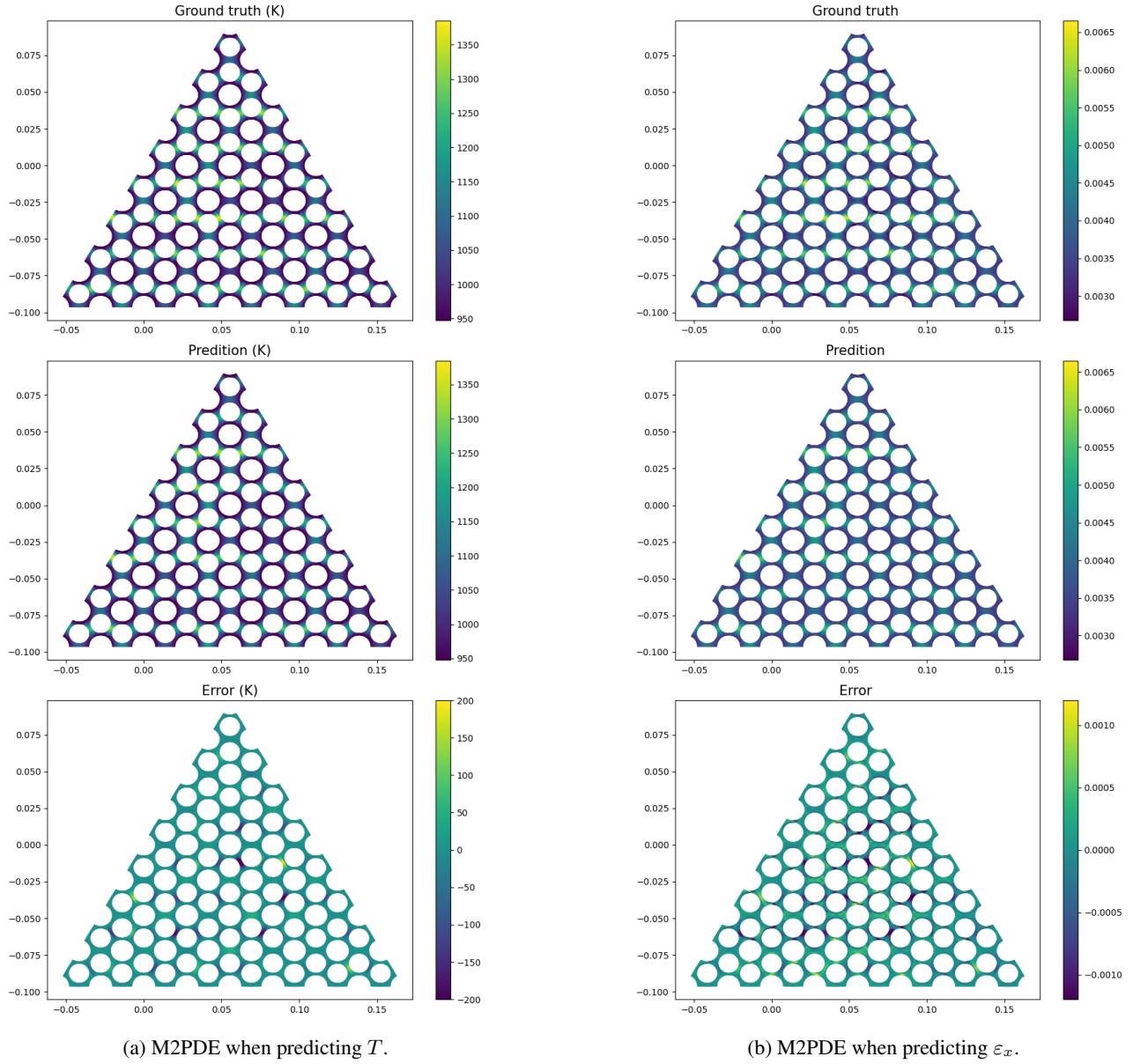
(b) M2PDE when predicting ε_x.

Figure 11. The results of M2PDE + FNO for predicting large structure.

Table 8. Hyperparameters of model architecture for prismatic fuel element task.

Hyperparameter name	
Hyperparameters for Transolver	
Number of layers	5
Number of head	8
Number of slice	16
Hidden dim	64
Hyperparameters for Geo-FNO	
Uniform grid size	[64, 64]
FNO width	5
FNO mode	[8,8]
Number of FNO layer	3
Hidden dim	64

Table 9. Hyperparameters of training for prismatic fuel element task.

Hyperparameters for Transolver and Geo-FNO training	
Loss function	MSE
Number of examples for training dataset	16000
Total number of training steps(surrogate;diffusion)	$10^5; 2 \times 10^5$
Gradient accumulate every per epoch	2
learning rate	10^{-4}
Batch size	256

E. Comparison of models trained using coupled and decoupled data.

To further investigate the model's boundaries for multiphysics simulation, we utilize coupled data to train diffusion models and compare them to models trained on decoupled data in experiments 1 and 2. The input of the diffusion model is the external input of the physical system, while the output is the solution of the coupled physical fields. In experiment 1, the input consists of the initial conditions of u and v, with the output being their trajectories. Since u and v are defined on the same grid, a single network can be employed to predict u and v together. In experiment 2, the input is the variation of neutron boundaries over time, and the output is the trajectories of the neutron field, solid temperature , and fluid fields. Since that the three fields are defined in different computational domains, three separate networks are trained. Aside from the differences in input and output dimensions, all other parameters remained consistent with those used in the decoupled scenario. The coupled datasets for experiments 1 and 2 consist of 10,000 and 5,000 samples, respectively, which is consistent with decoupled datasets. The model is evaluated using unseen coupling data during training.

The result is shown in Table 10, the accuracy of the model trained with decoupled data decreased by about 1 order of magnitude.

Table 10. Comparison of models trained on coupled and decoupled data.

	Coupled data model	Decoupled data model
Reaction-diffusion		
u	0.00151	0.0141
v	0.00185	0.0174
Nuclear thermal coupling		
neutron	0.00512	0.0197
solid	0.00098	0.0287
fluid	0.00302	0.0391

F. ABLATION STUDY

F.1. Method for calculating the estimated physical fields

We compare two methods for estimating physical fields: one using z_i^e from Eq. 9 and the other using the current physical field $z_{i,s}$ with noise. As shown in Table 11, z_i^e provides significantly better results than $z_{i,s}$, indicating that the estimate from z_i^e is more accurate.

Table 11. Comparison of methods for estimating physical fields.

	$z_{i,s}$	z_i^e(Eq.9)
Reaction-diffusion		
u	0.0525	0.0141
v	0.0355	0.0174
Nuclear thermal coupling		
neutron	0.0184	0.0197
solid	0.0913	0.0287
fluid	0.1000	0.0391
Prismatic fuel element		
T	0.0289	0.0076
ε	0.0083	0.0194

F.2. Selection of Hyperparameter K

This section examines how hyperparameter K affects the predictive performance of multiphysics and multi-component problems in experiments 2 and 3. As shown in Tables 12 and 13, setting K to 2 for multiphysics problems and K to 3 for multi-component problems is adequate. The multiphysics algorithm updates physical fields at each diffusion time step, leading to faster convergence. In contrast, the multi-component problem relies on the field estimated in the previous time step for each diffusion iteration, resulting in slower convergence. Additionally, increasing K further has a negligible effect on model performance.

Table 12. Hyperparameters of K for multiphysics simulation.

K	neutron	solid	fluid
1	0.0199	0.0304	0.0524
2	0.0206	0.0287	0.0391
3	0.0203	0.0288	0.0395

Table 13. Hyperparameters of K for multi-component simulation.

K	T	ε
1	0.00907	0.0236
2	0.00833	0.0222
3	0.00785	0.0206
4	0.00772	0.0207
5	0.00750	0.0203

F.3. Selection of Hyperparameter of λ

The hyperparameters λ determine the weight of the current physical field, theoretically requiring a reliable estimate of 0 at the beginning and gradually increasing to 1 as diffusion progresses to provide better estimates of the current results in the later stage. We demonstrate this with experiment 3, which involves solving 64 components with slow convergence, making it sensitive to hyperparameter λ. We set the values to 0, 1, 0.5, and a linear increase. When K is too large, result differences

are minor, except when λ is 1; thus, K is set to 2. As shown in Table 14, employing a linearly increasing setting yields superior performance, which is consistent with the analysis.

Table 14. Hyperparameters of λ for multi-component simulation.

λ	T	ε
0	0.00878	0.0228
1	0.00913	0.0237
0.5	0.00895	0.0233
linear increase	0.00816	0.0217

G. The difference between training dataset and testing dataset.

For multiphysics simulation, we train models for each physical process using decoupled data and combine them during testing to predict coupled solutions; for multi-component simulation, we train a model to predict individual component, then combine it during testing to predict the large structure composed of multiple components. To quantify the difference between the model's training and testing data, we calculate the Wasserstein distance (Feydy et al., 2019) between the training and validation data, as well as between the training and testing data, with the training and validation data originating from the same distribution. In addition, we also used the t-SNE (Van der Maaten & Hinton, 2008) algorithm to visualize this difference.

The results are presented in Table 15. In experiment 1, there is a significant difference between the training and testing data, as can be seen from Fig. 12, where only a small fraction of decoupled data points fall within the range of coupled data. In experiment 2, the difference between the training and testing data for the neutron physics field is relatively small, likely due to the weak coupling effect of other physical processes on the neutron physics field. For the solid temperature field and fluid field, the difference between the training and testing data is also very pronounced, with almost no overlapping points in the Fig. 13. In experiment 3, since the range of training data has been expanded during data generation to cover as many potential scenarios of large structures as possible, the difference between the training and testing data is not as significant as in the multiphysics problem, and the testing data are also within the range of the training data, as shown in the Fig. 14.

Table 15. Wasserstein distance of datasets.

	Training and validation	Training and testing
Reaction-diffusion		
u	0.343	52.7
v	0.0435	20.3
Nuclear thermal coupling		
neutron	42.4	31.3
solid	1.35	56.3
fluid	1.22	986
Prismatic fuel element		
T	0.233	9.05
ε	0.625	12.5

(a) u.

(b) v.
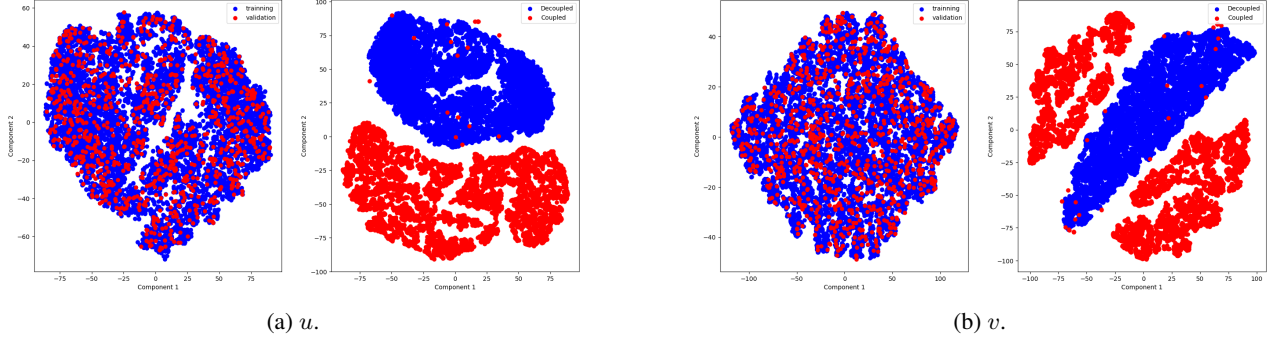
Figure 12. Visualization of experiment 1 Dataset.

(a) Neutron.

(b) Solid.

(c) Fluid.
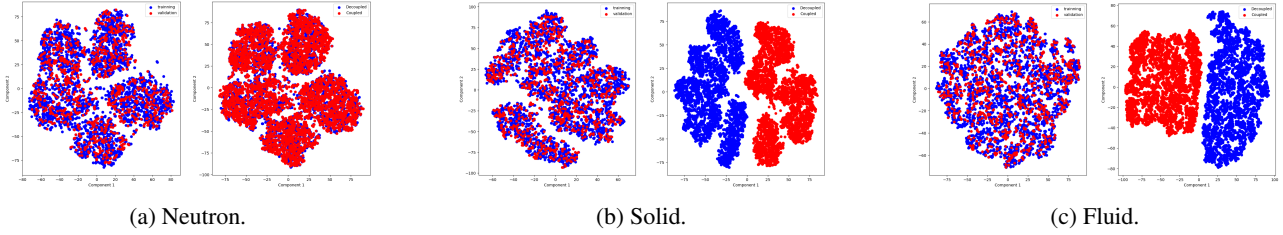
Figure 13. Visualization of experiment 2 Dataset.

(a) T.

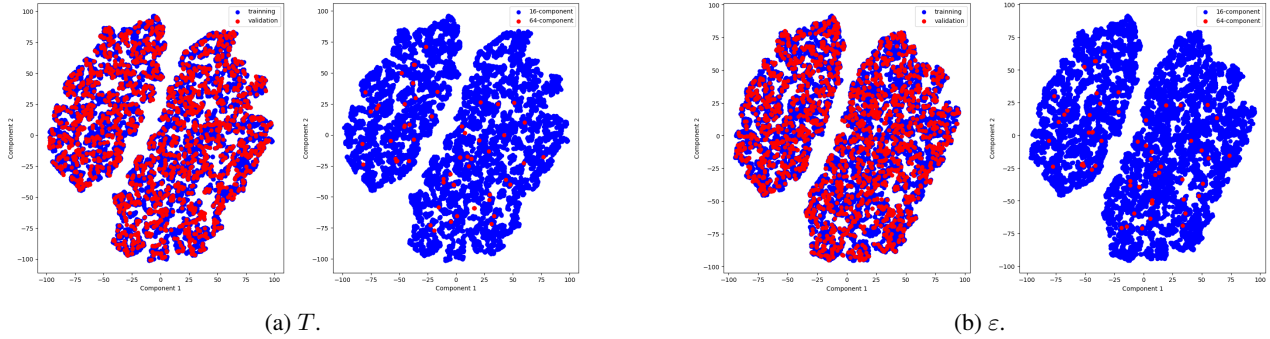(b) ε.

Figure 14. Visualization of experiment 3 Dataset.

H. Sampling acceleration.

By employing the DDIM algorithm to expedite the sampling process of diffusion models, we have successfully enhanced the efficiency of model inference. The DDIM algorithm encompasses two parameters: the number of time steps S and the parameter η, which controls the noise (Song et al., 2021):

$$\sigma_t = \eta \sqrt{\frac{1 - \overline{\alpha}_{t-1}}{1 - \overline{\alpha}_t} \beta_t} \tag{19}$$

where $\eta \in [0, 1]$. We conduct tests across various parameter combinations, including $S = 10, 25, 50$, and $\eta = 0, 0.5, 1$, with a particular focus on the model's performance in coupled and large structure prediction. These three experiments all use the most accurate model, which is: U-Net, U-Net, Transolver. Table 16 indicates that in experiment 1, the setting of $S = 25$ closely mirrors the results of $S = 50$, with η having a relatively minor impact. Table 17 indicates that in experiment 2, the setting of $S = 25$ also approximates the outcome of $S = 50$ but is more sensitive to η, with $\eta = 1$ yielding the best performance. Table 18 indicates that in experiment 3, $S = 50$ is the optimal setting, and $\eta = 0$ provides the best results.

During the training of diffusion models, we uniformly set the number of time steps to 250. By employing accelerated

sampling techniques, we achieved a 10-fold acceleration for multiphysics problems and a 5-fold acceleration for multi-component problem while ensuring the maintenance of predictive accuracy.

Table 16. Relative L2 norm of error on reaction-diffusion equation for DDIM sampling.

method	u decoupled	coupled	v decoupled	coupled
Original DDPM	0.0119	0.0141	0.0046	0.0174
$S = 10, \eta = 0$	0.0143	0.0170	0.0117	0.0215
$S = 25, \eta = 0$	0.0123	0.0151	0.0082	0.0190
$S = 50, \eta = 0$	0.0123	0.0147	0.0059	0.0179
$S = 25, \eta = 0.5$	0.0123	0.0152	0.0082	0.0191
$S = 25, \eta = 1$	0.0119	0.0151	0.0081	0.0192

Table 17. Relative L2 norm of prediction error on nuclear thermal coupling for DDIM sampling. The unit is 1×10^{-2}.

method	**neutron** decoupled	coupled	**solid** decoupled	coupled	**fluid** decoupled	coupled
Original DDPM	0.487	1.97	0.108	2.87	0.303	3.91
$S = 10, \eta = 1$	0.638	1.89	0.261	4.45	0.478	4.42
$S = 25, \eta = 1$	0.552	2.03	0.142	3.64	0.343	4.08
$S = 50, \eta = 1$	0.533	1.96	0.138	3.21	0.346	4.02
$S = 25, \eta = 0.5$	2.82	2.78	0.793	5.28	0.970	4.70
$S = 25, \eta = 0$	10.9	10.3	2.99	14.4	1.82	8.20

Table 18. Relative L2 norm of prediction error on prismatic fuel element experiment for DDIM sampling. The unit is 1×10^{-2}.

method	**single** T	ε	**16-component** T	ε	**64-component** T	ε
Original DDPM	0.107	0.303	0.213	1.03	0.759	1.94
$S = 10, \eta = 0$	0.207	0.425	1.69	3.81	1.89	4.13
$S = 25, \eta = 0$	0.166	0.353	0.952	2.55	1.30	3.26
$S = 50, \eta = 0$	0.158	0.337	0.669	1.87	0.865	2.31
$S = 50, \eta = 0.5$	0.150	0.352	0.586	1.69	0.954	2.61
$S = 50, \eta = 1$	0.130	0.322	0.553	1.62	1.05	2.80

I. Efficiency analysis.

This section compares the computational efficiency of M2PDE, surrogate model, and numerical programs. The time unit for each experiment is defined as the time required for a single neural network inference. These three experiments all use the most accurate model. Since the surrogate model and M2PDE both use the same network architecture and have consistent network parameters, it is assumed that the time for a single inference using these two methods is equal. The numerical programs are run on the CPU and have all been optimized to the best parallel count.

Let the number of physical processes be denoted by N, the number of iterations for the surrogate model by M, the number of diffusion steps by S, and the number of outer loop iterations for the diffusion model by K. The computation time for the surrogate model is $M \times N$, while the diffusion model is $K \times S \times N$. The specific choices of N, M, S, K for each experiment are presented in Table 19.

The results are presented in Table 20. In experiment 1, the problem is relatively simple, and the numerical algorithm achieves efficient solutions through explicit time stepping, while the introduction of M2PDE actually reduces efficiency. However, in experiment 2, which addresses more complex problems, M2PDE achieves a 29-fold acceleration compared to numerical programs. In experiment 3, comparing the results of 16 components with 64 components, it is observed that as the computational scale increases, the acceleration effect of M2PDE becomes increasingly significant. Furthermore, when dealing with multi-component problems, the surrogate model requires iteration to ensure the convergence of solutions across all components. Due to the large number of components, the number of iterations needed significantly increases compared to multiphysics problems, resulting in higher efficiency for M2PDE. In addition, we have only compared the efficiency of single computations for all experiments. When dealing with multiple problems simultaneously, the acceleration provided by M2PDE will be even more pronounced due to the parallel nature of GPU computing.

In general, the more complex the problem, the more pronounced the acceleration effect of M2PDE becomes. In fact, the problems in experiment 2 and experiment 3 have been simplified to a certain extent, and the actual situations are even more complex. Therefore, M2PDE holds significant value in solving real-world complex engineering problems.

Table 19. Values of K, N, M, and S for the three experiments.

experiment	N	M	S	K
Reaction-diffusion	2	27	25	2
Nuclear thermal coupling	3	21	25	2
Prismatic fuel element (16-component)	1	309	50	3
Prismatic fuel element (64-component)	1	324	50	3

Table 20. Comparison of running time.

Experiment	Unit (s)	Numerical program	Surrogate model	M2PDE	Speedup
Reaction-diffusion	0.0115	6	54	100	0.064
Nuclear thermal coupling	0.0242	4368	63	150	29
Prismatic fuel element (16-component)	0.0067	834	309	150	5.6
Prismatic fuel element (64-component)	0.0256	6170	324	150	41

J. Application Scenarios for Multi-Component simulation.

In this section, we discuss the application scenarios of M2PDE for multi-component simulation from both theoretical and practical perspectives.

From a theoretical perspective, in the derivation of Section 3.2, we make an assumption: the solution on a multi-component structure is an undirected graph that satisfies the local Markov property, meaning that any two non-adjacent variables are conditionally independent given all other variables. Using this property, we derived Eq. 14. We believe this assumption is applicable to most problems because physical fields are continuous in space, and the information exchange between any two points must be transmitted through the points in between. However, there is a class of problems to which current methods cannot be directly applied, which is the PDE that requires determining eigenvalues:

$$\mathbf{M}\phi = \lambda\phi \tag{20}$$

Here $\mathbf{M}$ is the operator, λ is the eigenvalue, ϕ is the physical field to be solved. The λ varies with different systems, and the relationships we learn on small structures may not be applicable to large structures. Solutions to these problems may be similar to numerical algorithms, requiring the addition of an eigenvalue search process, which will be undertaken in future work.

From a practical implementation perspective, for a complex structure, it is necessary to clearly determine its basic components and the relationships between these components and their surrounding components, so that we can understand how the

components are affected by their surrounding components. In addition, training data must encompass all possible scenarios that each component in a large structure might encounter, such as all possible boundary conditions and the relationships with surrounding components.

K. Datasets Description.

This section provides a concise description of the datasets utilized in the three experiments, with their detailed backgrounds introduced in Appendix B, C, D. We outline the principal characteristics of these datasets and compare them with the standard scientific datasets PDEbench (Takamoto et al., 2022). Comparison is shown in Table 21, where N_d is the spatial dimension, N_f is the number of physical processes, and N_c is the number of components. Table 21 only lists some of the datasets in PDEBench, but all of its datasets have N_f and N_c values of 1. The dataset of Experiment 1 in this paper exists in the benchmark, but Experiments 2 and 3 are completely new datasets.

Table 21. Datasets Description.

PDE	N_d	Time	Computational domain	N_f	N_c
Burgers'	1	yes	Line	1	1
compressible Navier-Stokes	3	yes	Cube	1	1
incompressible Navier-Stokes	2	yes	Rectangle	1	1
shallow-water	2	yes	Rectangle	1	1
reaction-diffusion (Exp1)	1	yes	Line	1	1
heat conduction + neutron diffusion + incompressible Navier-Stokes (Exp2)	2	yes	3 Rectangle	3	1
heat conduction + mechanics (Exp3)	2	no	Irregular domain	2	16 , 64